Model for optimal management of the cooling system of a fuel cell-based combined heat and power system for developing optimization control strategies

F.J. Asensio[a], J.I. San Martín[a*], I. Zamora[b], O. Oñederra[b]

[a]Electrical Engineering Department, Engineering School of Gipuzkoa (Section of Eibar), University of the Basque Country UPV-EHU, Eibar 20600, Spain
[b]Electrical Engineering Department, Engineering School of Bilbao, University of the Basque Country UPV-EHU, Bilbao 48013, Spain
*Corresponding author: joseignacio.sanmartin@ehu.eus

A B S T R A C T

This paper is focused on the development of a model for achieving optimal control of the cooling system of a polymer electrolyte membrane fuel cell (PEMFC)-based cogeneration system. This model is developed to help facilitate the development and application of control strategies to maximize the energy efficiencies of PEMFCs, so that the costs associated with electric and thermal generation can be reduced. The results of experimental analysis conducted using an actual PEMFC-based combined heat and power system that can produce 600 W of electrical power are presented. Then, the development and validation of a simulation model of the experimental system are discussed. This model is based on a combination of an artificial neural network (ANN) with a non-linear autoregressive exogenous configuration and a 3D lookup table (LUT) that updates the data input into the ANN as a function of the electrical power demand and the flow rate and input temperature of the coolant fluid. Due to the nonlinearity of the data contained in the 3D LUT, an algorithm based on linear interpolation and shape-preserving piecewise cubic Hermite dynamic functions is implemented to interpolate the data in 3D. As a result, the model can predict the outlet temperature of the coolant fluid and hydrogen consumption rate of the PEMFC as functions of the inlet temperature and flow rate of the coolant fluid and the electrical power demand. The proposed model exhibits high accuracy and can be used as a black box for the development of new optimization strategies.

Keywords

Polymer electrolyte membrane fuel cell (PEMFC), Combined heat and power (CHP), Cooling system management, Optimal control, Energy efficiency prediction.

Nomenclature

A	Cross-sectional area of the cooling circuit inlet
A_s	Stack surface area exposed to the ambient
B_i	Elements of Bernstein polynomials
C_p	Specific heat at constant pressure
D_h	Hydraulic diameter
F	Volume force vector
h	Heat transfer coefficient
h_{ii}	Basic Hermite functions
I	Identity matrix
k	Thermal conductivity
L	Height of the stack
m	Tangent
$\dot{m}$	Mass flow
Nu	Nusselt number
p	Fluid pressure
P_w	Wetting perimeter
P	Power
Pr	Prandtl number
q	Conductive heat flux
Q	Heat
Ra	Rayleigh number
Re	Reynolds number
S	Strain rate tensor
t	Time
T	Temperature
u	Fluid velocity vector
v	Kinematic viscosity
V	Stack volume

Acronyms

ANN	Artificial neural network
CHP	Combined heat and power
DC	Direct current
FC	Fuel cell
FEM	Finite element method
LUT	Lookup table
NARX	Nonlinear autoregressive exogenous
PCHIP	Piecewise cubic Hermite interpolating polynomial
PEMFC	Polymer electrolyte membrane fuel cell
SLPM	Standard litres per minute
SVM	Support vector machines

Greek symbols

α_p	Thermal expansion coefficient
∇	Fluid divergence
Δ	Slope of secant line
ρ	Density
τ	Tensor of viscous forces
μ	Dynamic viscosity

Subscripts

a	Ambient
bl	Boundary layer
conv	Convection
el	Electrical
in	Inlet
out	Outlet
s	Surface
th	Thermal power

1. Introduction

The need to improve energy production systems has led to the development of more efficient and smaller distributed generation technologies that use energy from renewable sources and cogeneration cycles. In this context, the most frequently employed technologies are internal combustion engines, gas micro-turbines, Stirling engines, and fuel cells (FCs) [1], [2].

Among all combined heat and power (CHP) technologies, FCs stand out because they use energy resources effectively owing to their high efficiencies [3]. They also allow the use of different fuels from very different primary resources that favour integration with renewable modalities. Among all existing types of FCs, polymer electrolyte membrane FCs (PEMFCs) show great potential for integration into CHP systems [4]–[6]. Among the characteristics of PEMFCs, fast dynamics, low operating temperatures, high efficiencies at partial load, high power densities, and easy scalability are particularly notable [7].

To operate a CHP system optimally, it is essential to develop models and operation strategies that take into account fuel price and electric tariff variations, which significantly affect the operating costs of CHP systems. There are several operational strategies for CHP system operation, the most commonly employed being the electricity-led, heat-led, time-led, peak saving, and load levelling strategies. Taking into account the costs associated with electricity, fuel, operation, maintenance, start-up, shutdown, etc., by means of one operational strategy or another, the objectives are to maximize the energy efficiency and minimize the total system costs.

In the current literature, several works that present models, operation modes, and optimization strategies intended to improve the efficiencies and reduce the costs of CHP systems can be found [8]–[21]. However, the vast majority focus on CHP systems that are not expressly based on FCs, so the models used do not adjust with sufficient accuracy to the characteristic behaviour of this technology.

The simulation model employed is a key factor when developing an optimal operation strategy for a PEMFC-based CHP system, so it must be able to predict the electrical and thermal efficiencies of the FC under different operating conditions with sufficient accuracy. It should be noted that the efficiency of an FC depends mainly on the electric power generated and operating temperature [22]. Furthermore, it must be taken into account that as the electrical power increases, so do the consumptions of several auxiliary elements to maintain the necessary electrochemical reactions, such as the hydrogen and air compressors, which lowers the electrical efficiency. On the other hand, as the operating temperature increases, the kinetic reactions in the catalysts are improved and the electrochemical conductivity of the membrane is increased, which leads to a higher electrical efficiency. The operating temperature also affects the degradation of the PEMFC components, particularly the membrane-electrode assembly [23], [24]. However, if the nominal operating temperature (~80 °C) is not exceeded, the contribution of the temperature to the degradation of the electrolyte can be assumed to be insignificant [25].

Another aspect influenced by the operating temperature is related to the formation and transport of the water obtained as a by-product of the electrochemical reactions. However, the effects of water on PEMFC degradation can be practically eliminated by using advanced materials or effective strategies for water management in cells [26], [27].

There are several cooling methods for controlling the operating temperature of a PEMFC, such as cooling by increasing airflow at the cathode, cooling by forced ventilation, cooling by using dissipating surfaces, liquid cooling, and phase-change cooling [28], [29]. However, for a PEMFC-based CHP system, the refrigeration system must allow for the recovery of the waste heat extracted from the FC stack. The usable systems include liquid and phase-change cooling systems. Although phase-change cooling systems have some advantages over liquid cooling systems, if the PEMFC is integrated into a CHP system, a liquid refrigeration system is more appropriate due to the greater cooling capacities and greater flexibility in terms of the control of such systems [28].

Bearing in mind all of the above, it can be assumed that the operating temperature of a PEMFC can be managed by controlling the cooling system within the operation limits in order not to compromise the materials, so the temperature only affects the energy efficiency of the system.

On one hand, if a PEMFC system is operated using an electricity-led strategy, the electrical efficiency could be optimized simply by keeping the stack temperature as high as possible, within the operating limits. Thus, the refrigeration system is only required to maintain the nominal temperature of the PEMFC, and the surplus heat is released through the cooling circuit regardless of the thermal demand. On the other hand, if the PEMFC system is operated under a heat-led strategy, the PEMFC and its cooling system will have to be controlled to extract the amount of heat necessary to cover the thermal demand, regardless of whether or not the electrical efficiency is affected by the operating temperature. However, if the PEMFC is connected to a grid and integrated with other heat and/or power generation devices, the optimization strategy is more complex. In this sense, taking into account variable fuel and electricity prices, the operating and maintenance costs of all of the devices,

etc., the PEMFC must be operated at a specific point to obtain a relationship between the electrical and thermal production that minimizes the total cost of the system. To identify this optimum operating point at each instant, it is necessary to know the electrical and thermal efficiencies of the PEMFC for each load factor, the amount of heat extracted by the cooling circuit, and the operating temperature.

Numerous studies have been conducted in which FC models were applied in strategies intended to optimize PEMFC-based cogeneration systems [30]–[41]. However, simplified FC models or models in which the FC efficiency depended only on the electrical power generated were employed in most of those studies, and the effects of the temperature on the electrical and overall efficiencies of the systems were not considered. Shaverdi et al. [42] proposed a model in which the electrical efficiency is defined in three sections, depending on the electric power demand and recovered thermal power. However, the model does not include the possible variation of the heat extracted from the FC by the management of the cooling system. Hawkes et al. [43], [44] proposed a model that predicts linear degradation of the electric efficiency of the FC in proportion to the electrical energy demand and thermal cycles. However, for a given degree of degradation, the effect of the operating temperature on the efficiency of the system is not considered. Arsalis et al. [45], [46] and Merechal et al. [47] proposed a model in which the efficiency varies with the stack temperature. However, the temperature is taken as an input variable independent of the operating conditions, so the model is not able to simulate the effects of temperature on efficiency, depending on the energy demand. Najafi et al. [48] also proposed a model that includes the variation of the electrical efficiency as a function of the operating temperature. To do so, they defined the membrane conductivity parameter as a function of temperature. However, this model does not calculate the temperature as functions of the electrical demand and the flow rate and input temperature of the coolant fluid.

The authors of this research work presented in [49] a PEMFC model based on an artificial neural network (ANN) with a nonlinear autoregressive exogenous (NARX) configuration, which can provide the coolant outlet temperature and hydrogen consumption rate as functions of the electrical demand, thermal demand, coolant inlet temperature, and coolant flow rate. However, the physical system used to train the ANN is a closed system in which the coolant flow rate is restricted by software to a very limited range, 0.99–1.07 l/min, to protect the PEMFC system from overheating and to avoid degradation or destruction of its components. Thus, the model proposed in [49], despite yielding highly precise results, cannot accurately predict the electrical and thermal efficiencies of PEMFC systems for coolant flow rates that are not within the range for which the model was configured.

Taking into account all of the above, the need to develop a PEMFC system model that provides the electrical and thermal efficiencies as functions of the electrical production and heat extracted from an FC system by controlling the coolant flow rate is evident. Therefore, this paper presents a novel PEMFC-based CHP system model that facilitates optimal operation by controlling the cooling circuit and will facilitate the development and testing of new optimization strategies.

2. Experimental analysis

This section presents the PEMFC-based CHP system used to conduct the laboratory tests, as well as the experimental results obtained for the development and validation of the model.

2.1. PEMFC-based CHP system

The laboratory tests were performed using an HP600 system, which consists of a PEMFC-based CHP system that can produce 600 W of electrical power. Fig. 1 shows the operating scheme of the HP600 system.
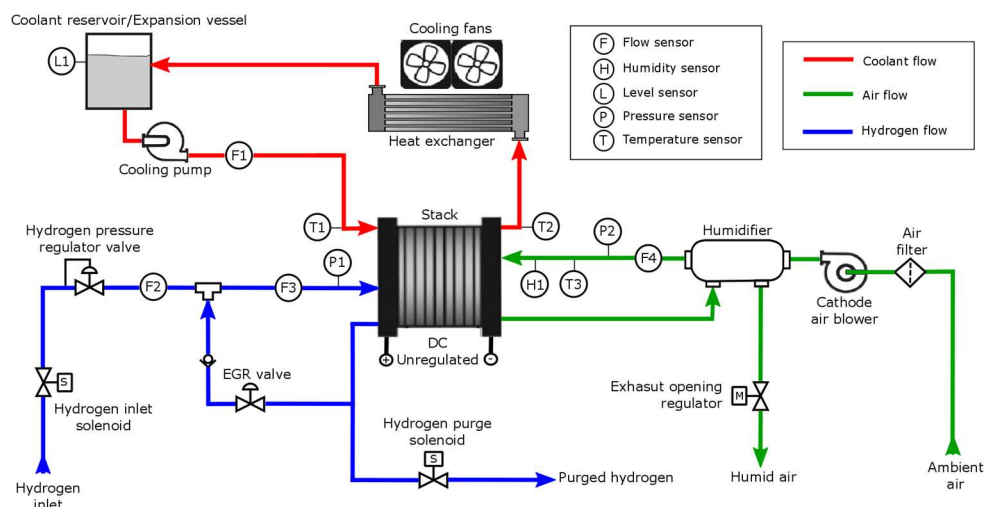

Fig. 1. Operating scheme of the HP600 system.

The FC stack consists of 24 cells connected in series. The electrical power produced is extracted through two external terminals. Some of this power is consumed in internal processes within the equipment itself. The remaining power can be applied to external loads.

The HP600 FC system is designed to operate with high-purity hydrogen and atmospheric oxygen. The electrically regulated cathode fan takes air from the environment through a filter and inputs it into the FC stack through the membrane humidifier. The humidifier uses return air mixed with by-product water from the electrochemical reactions. Once used in the humidifier, leftover water is released into the environment as moist air, through an exhaust opening. A servo-controlled valve regulates the cross-section of the exhaust opening.

Hydrogen enters the stack from the hydrogen source through the inlet hydrogen solenoid and a pressure-reducing valve. The exhaust gas recirculation valve returns unreacted hydrogen to the inlet. Excess hydrogen, or contaminated hydrogen, is expelled from the circuit by the purging solenoid.

A liquid cooling circuit based on demineralized water recovers the heat produced in the exothermic reactions. An electric pump introduces the fluid into the stack, collects heat, and then releases it into the environment through a fluid/air heat exchanger. The degree of heat extraction is controlled by forced ventilation by two electrically regulated fans. Table 1 lists the most relevant characteristics of the HP600 PEMFC-based CHP system.

Table 1. Technical specifications of the HP600 system.

Parameter	Value
DC unregulated output voltage	13.5–22 V_{DC}
Rated current	45 A
Rated voltage	14.4 V
Short-circuit voltage	23.5 V
Rated hydrogen pressure	4–8 bar (regulated by pressure valve)
Ambient operation temperature range	15–35 °C
Operation temperature	45–60 °C
Active area	24 cells, 130 cm^2 each
Cooling fluid	Demineralized water (conductivity < 1uS/cm)
Hydrogen purity	>4.0 (99.99% purity) or hydrogen 3.0 from electrolyser (sulphur compounds and other poisonous components are not allowed)
Hydrogen flow rate @ rated power	9 SLPM

2.2.   Experimental results

To study the thermal behaviour of the PEMFC-based CHP HP600 system and to obtain data for the development and validation of the model, several laboratory tests were conducted while varying the electric power consumed and heat extracted from the stack through the cooling circuit. Fig. 2 shows the equipment used in the laboratory tests.
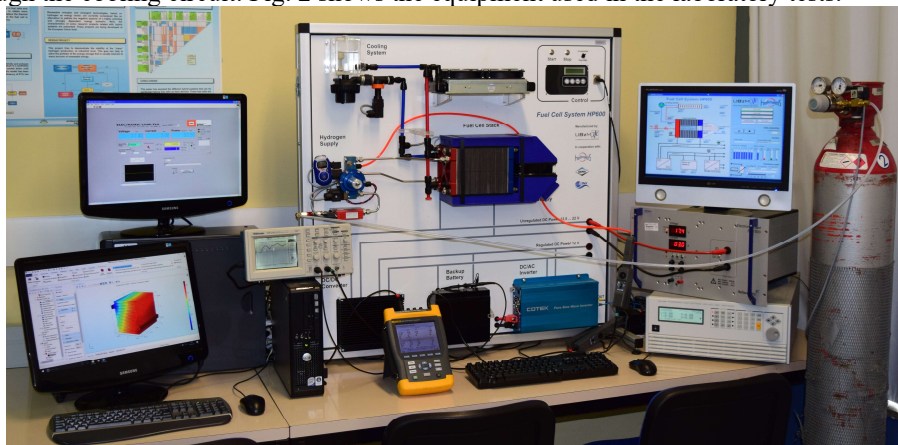

Fig. 2. Equipment used in the laboratory tests.

To determine the effects of the temperature variations of the stack and coolant outlet fluid as functions of the electric demand and heat extracted from the stack, different electrical powers were demanded by the EL-1500 programmable electronic load. For each electrical power, a different amount of heat was extracted from the stack. Under these conditions, the stack temperature, coolant inlet and outlet temperatures, coolant and hydrogen flow rates, electrical power consumed (including auxiliary services), and heat extracted from the stack were recorded.

Fig. 3(a) shows the results for the electric power demanded, heat extracted from the stack, and coolant flow, and Fig. 3(b) shows the results for the heat extracted from the stack and the coolant inlet and outlet temperatures.
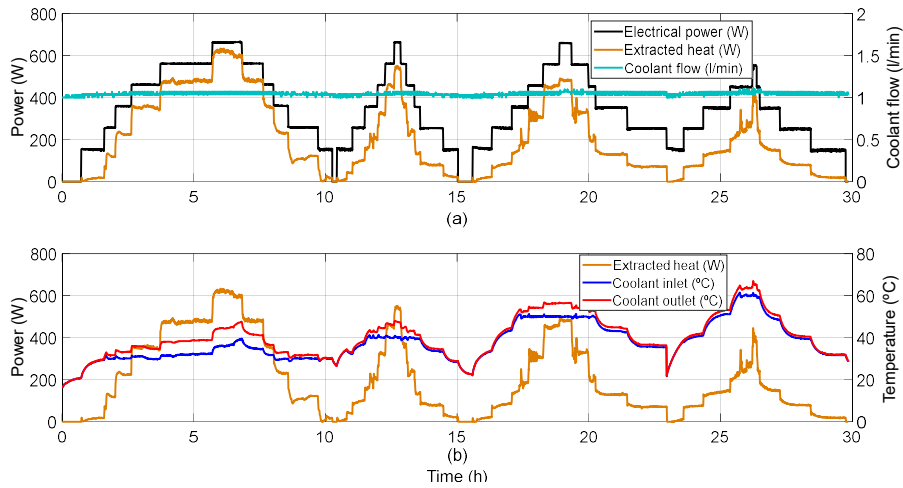
Fig. 3. (a) Electrical power, heat extracted, and coolant flow rate and (b) heat extracted and coolant inlet and outlet temperatures.

To observe the efficiency variation as a function of the stack temperature, the current through the HP600 system was swept from 0 A to 50 A. After reaching the maximum current, heat was extracted from the stack until the temperature had stabilised. After temperature stabilisation, the current was reduced again from 50 A to 0 A. Fig. 4 shows the electrical power demanded from the system, the thermal power extracted from the stack, the electrical efficiency of the system, and the stack temperature in this test.
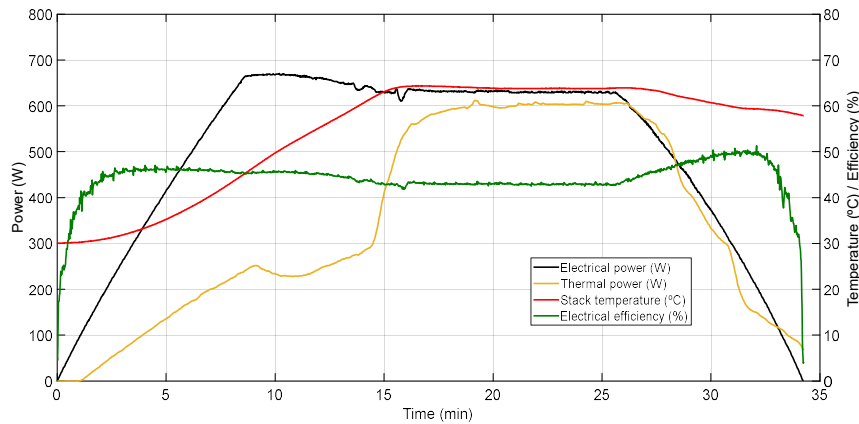
Fig. 4. Electrical power, heat extracted, electrical efficiency, and stack temperature obtained from the current sweep test.

Fig. 4 shows that the electrical efficiency depends on the stack temperature and increases with increasing temperature. For example, for a power of 200 W, two different electrical efficiencies were obtained. During the current increase, an efficiency of 44.72% was obtained, corresponding to a temperature of 31.02 °C, while during the current decrease, the efficiency was 51.25%, corresponding to a temperature of 59.35 °C.

Fig. 5 shows the electrical, thermal, and global efficiencies of the system for the electric power demands and amounts of heat extracted in Fig. 3. Fig. 5 shows that different electrical efficiencies were obtained for the same electric power demand. The electrical efficiency changed during the test because the heat extracted from the stack differed when the same amount of electrical power was generated, so the stack temperature also differed. Consequently, if the heat extracted from the system is increased for the same electrical power demand, it is possible to reduce the temperature. Under these conditions, the thermal efficiency of the system increases considerably and the electrical efficiency decreases slightly. The maximum difference of the overall efficiency obtained for the same electrical power demand was 8.91%. At this point, the maximum overall efficiency was 91.8% (48.6% electrical and 43.2% thermal) and the minimum was 82.89% (48.17% electrical and 34.72% thermal). That is to say, extracting more heat from the system helped increase the thermal efficiency by 8.48%, while reducing the electrical efficiency by only 0.43%.
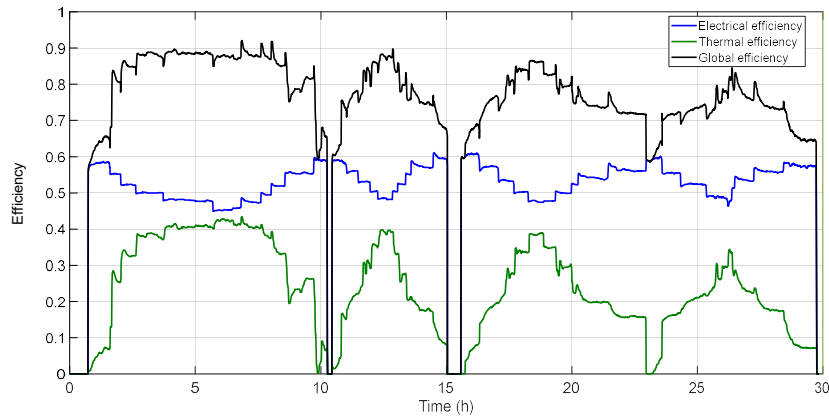
Fig. 5. Electrical, thermal, and overall efficiencies of the HP600 system.

The cooling system in this setup only allows heat extraction by forced convection by varying the electrically regulated fans of the liquid/air heat exchanger. This type of refrigeration system regulation is quite restrictive, since the system does not allow variation of the refrigerant fluid flow. Thus, the coolant flow rate remains essentially constant regardless of the power generated or the stack temperature.

If the coolant flow rate could be varied, the amount of heat extracted from the stack could be varied over a wider range. Specifically, the greater the range of heat extracted from the stack, the greater the range in which the stack temperature can be varied for the same electrical power generated. Assuming that the PEMFC system is connected to the grid and integrated with other auxiliary heat generation devices, this control would allow precise determination of the relationship between the electrical and thermal efficiencies at any time, so the total cost of the system could be minimized as functions of the electricity and fuel prices. Therefore, a model that considers the temperature variations and the effects of such variations on the system efficiency as a function of the electrical power demand and the flow rate and input temperature of the coolant fluid was developed.

3. PEMFC-based CHP system modelling

The model presented in this report is divided into two submodels. First, a thermodynamic submodel of the stack and cooling circuit calculates the coolant outlet temperature as functions of the flow and temperature of the cooling fluid and the electrical power demand. Then, the outlet temperature of the coolant is fed to an ANN-based submodel, together with the electrical power demand, to calculate the hydrogen consumption rate.

These two submodels are described separately below, as well as the integration of the submodels to form the complete model.

3.1. ANN-based submodel

Among the most popular artificial intelligence methods, such as ANNs, fuzzy logic systems, and support vector machines (SVMs), ANNs stand out as universal approximators that can be used to model highly nonlinear and time-dependent systems effectively [50], [51]. They enable users to abstract problems without requiring previous knowledge of the physical behaviour to be modelled, which is necessary in modelling based on fuzzy logic for correct definition of the functions or rules on which the problem is based [52]. The main competitors of ANNs are SVMs, which, like ANNs, provide very accurate results in highly nonlinear modelling [53]. However, Han et al. [54] demonstrated that ANNs are more effective than SVMs for emulating the behaviour of PEMFCs. Therefore, a modelling technique based on an ANN was employed in this research.

Among all existing ANN topologies, the NARX feedback configuration is effective when emulating the behaviour of a PEMFC integrated into a CHP system, as demonstrated previously [49]. The ANN used to implement this submodel is based on a serial–parallel autoregressive configuration with exogenous inputs and output feedback. Given the electrical demand and coolant outlet temperature, it provides the hydrogen consumption rate. Fig. 6 shows a schematic of the ANN-based model with the NARX-type configuration.
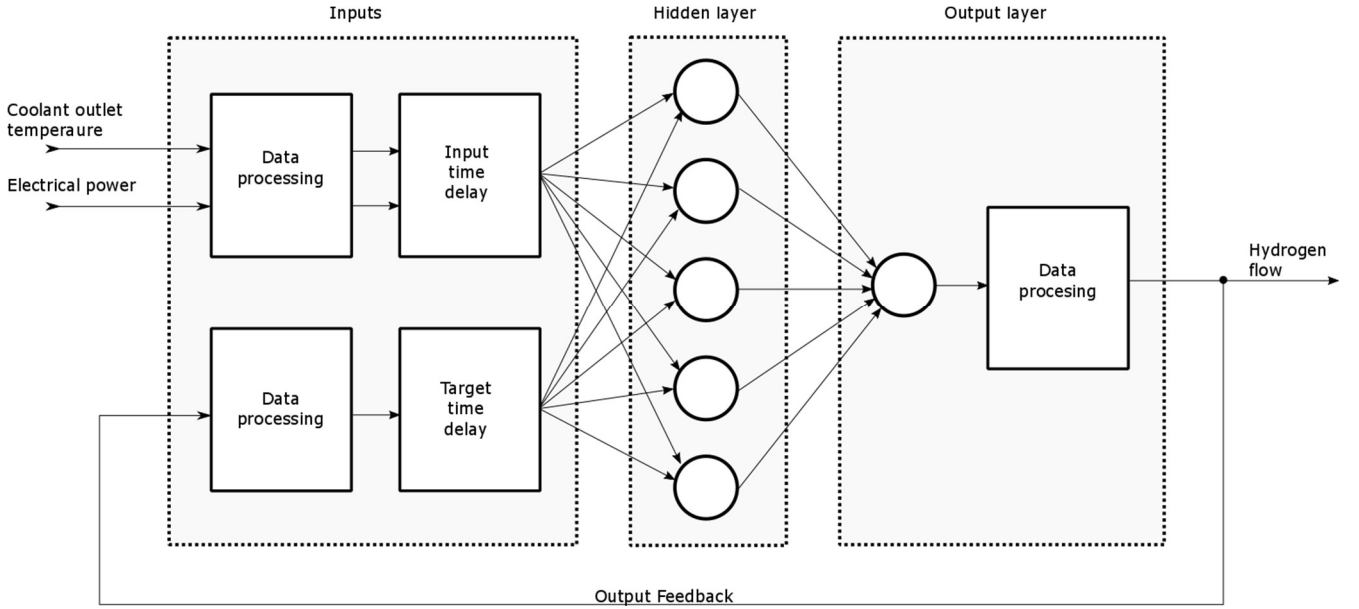
Fig. 6. PEMFC-based CHP model based on an ANN with a NARX configuration.

To reduce the generalization error of the ANN, a single hidden layer was considered. To obtain the optimum numbers of delay taps and neurons in the hidden layer, several configurations were trained using various values of such parameters. The employed training algorithm was based on the Levenberg–Marquardt algorithm [55], and the early stopping method was utilized to stop the training [56]. Of the 10,800 total samples, 70% were used for training, 15% for validation, and the remaining 15% for evaluation. Figs. 7(a) and 7(b) show the correlations obtained during training and evaluation of the optimum configuration, respectively.
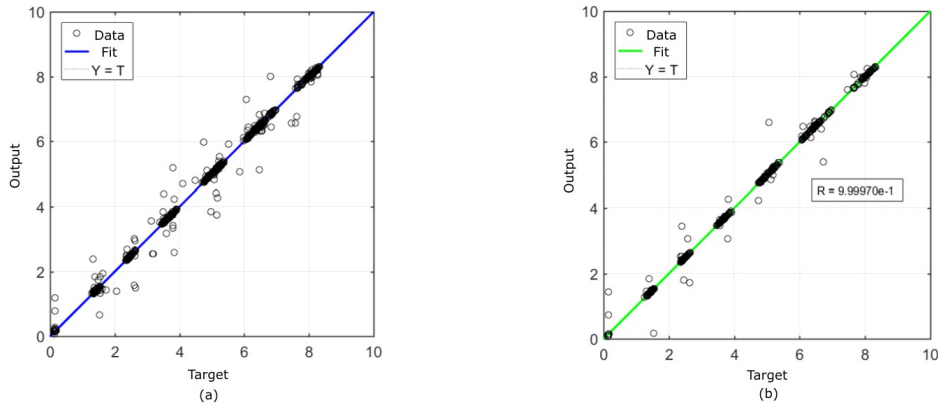
Fig. 7. Correlation of hydrogen flow rate by linear regression for (a) training and (b) validation.

The optimal configuration consists of two layers, the hidden layer, composed of 5 neurons, and the output layer, composed of 1 neuron. The mean squared error obtained for this configuration during evaluation was 5.75973e-4 at most.

The data input into the ANN were processed to normalize them in the range -1 to 1. This process was performed to avoid saturation of the transfer functions used in the neural network. Once the outputs were obtained, they were reprocessed to provide the data in the corresponding physical units. All input data, exogenous inputs, and endogenous outputs were delayed by up to two time units, so that the neural network obtained the new outputs from the inputs in one and two previous time units. The ANN outputs were calculated based on the inputs according to

$$y(k) = f\big(u(k-1), u(k-2), y(k-1), (k-2)\big), \tag{1}$$

where $y(k)$ is the value of the time series to be predicted at time step k; $u(k-1), u(k-2)$ and $y(k-1), y(k-2)$ are the values of the exogenous inputs and endogenous outputs, respectively, at time steps $(k-1)$ and $(k-2)$; and $f(\ )$ is the nonlinear function implemented.

The output $\boldsymbol{a_i^{n+1}}$ of each neuron $\boldsymbol{i}$ in layer $\boldsymbol{n+1}$ was obtained according to

$$a_i^{n+1} = f^{n+1}\left(\left(\sum_{j=1}^{k} W_{j,i}^{n+1} \cdot a_j^n\right) + b_i^{n+1}\right) \; for \begin{cases} n = 0, 1, \ldots, L-1 \\ i = 1, 2, \ldots, I \\ k = 1, 2, \ldots, K \end{cases}, \tag{2}$$

where L is the number of layers in the network, I is the number of neurons in the Lth layer, K is the number of inputs of the ith neuron in the Lth layer, $W_{j,i}^{n+1}$ is the weight applied to the jth input of the ith neuron, a_j^n is the output preceding the jth input, b_i^{n+1} is the bias applied to the ith neuron, and f^{n+1} is the transfer function used in the Lth layer.

The transfer functions used in the hidden layer ($L = 1$) and output layer ($L = 2$) are shown in (3) and (4), respectively:

$$f(x) = \frac{2}{1+e^{-2x}} - 1 \tag{3}$$

and

$$f(x) = x. \tag{4}$$

By modifying the previous version of the model presented in [49], the hydrogen consumption rate can be obtained regardless of the flow rate and inlet temperature of the coolant, because, as mentioned in Section 1, the previous model considers a very limited range of coolant flow variation, close to 1 l/min. Thus, the ANN can be configured so that the hydrogen consumption rate depends only on the electrical power and coolant outlet temperature. In this way, the operating point of the system can be optimized by means of the previous calculations of the cooling fluid output temperature as a function of the coolant inlet temperature, the electrical power demand, and a wide coolant flow rate range.

Section 3.2 describes the submodel that considers the dynamics of the cooling system. The objective of this submodel is to obtain the coolant outlet temperature to use it as an input for the ANN-based submodel. Then, the complete model obtained by coupling the two submodels that can predict the optimum operating point of the system is presented.

3.2. Cooling system thermodynamics submodel

Initially, geometric measurements were made using the HP600 system to determine the stack and internal cooling circuit dimensions. Then, the stack and cooling circuit geometries were implemented using the computer-aided design program called Solid Edge. Figs. 8(a) and 8(b) show the elevation, profile, plan, and isometric views of a bipolar plate with its respective cooling circuit channels and the assembly of the 24 cells forming the FC stack, respectively. The measurements in Fig. 8(a) are in millimetres.
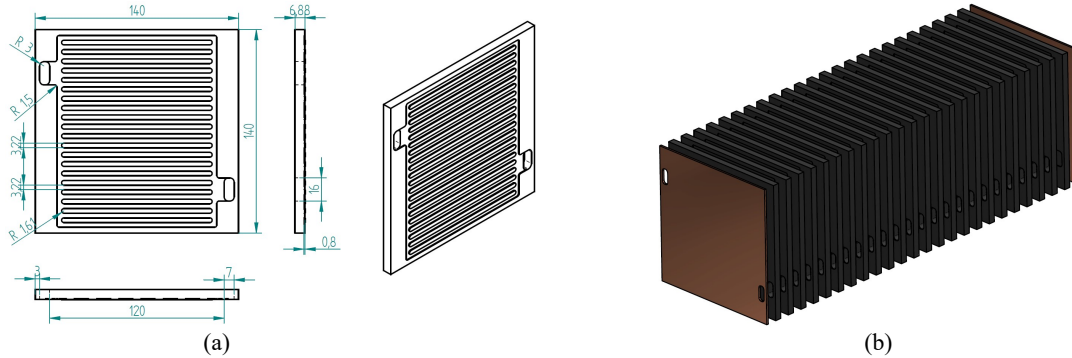

| (a) | (b) |

Fig. 8. (a) Bipolar plate elevation, profile, plan and isometric views and (b) the FC stack assembly.

Fig. 8(b) shows the anode and cathode current collectors covering the bipolar plates at the ends of the stack. Once the geometry was defined, it was exported to COMSOL Multiphysics software in IGES format. The domains of the cooling circuit and stack, as well as the materials of which each element was composed, were defined. Graphite was used for the stack, and water was used as the cooling fluid.

Once the stack and internal cooling circuit geometries had been obtained, they were meshed. After testing several mesh configurations, the configuration that yielded the highest accuracy and lowest computational cost was selected. Tetrahedral elements were used for the stack structure, and tetrahedral, pyramidal, and prism elements were employed for the cooling circuit. Table 2 summarizes the characteristics of the chosen mesh. Figs. 9(a), 9(b), and 9(c) show the FC stack geometry in the COMSOL environment, the cooling circuit mesh, and the stack mesh, respectively.

Table 2. Characteristics of the FC mesh.

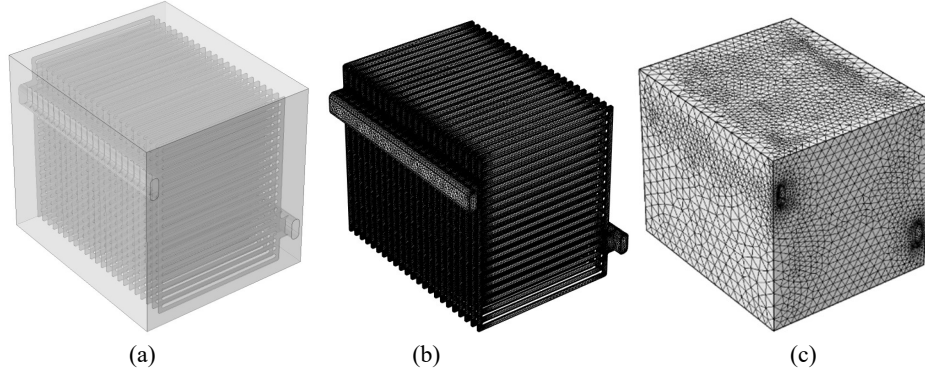| Parameter		Stack	Cooling circuit
Number of elements	Tetrahedral	1,228,805	312,916
	Pyramidal	0	5,414
	Prismatic	0	494,679
Minimum element quality		0.007548	1.099e-4
Average element quality		0.6996	0.195
Element volume ratio		6.511e-5	5.004e-4
Mesh volume		0.003071 m³	1.628e-4 m³

Fig. 9. (a) FC stack geometry in the COMSOL environment, (b) cooling circuit mesh, and (c) stack mesh.

Three physical principles were used to model the effects of varying the coolant inlet temperature and coolant flow rate on the stack temperature and coolant outlet temperature. The physics of heat transfer in solids was applied to the stack, and the physics of heat transfer in fluids and non-isothermal laminar flow were applied to the cooling circuit.

The formulation used to implement the three types of physics, as well as the integration and validation of the same applied to the stack and cooling circuit of the FC stack, is described below.

Inlet and outlet boundary conditions for the cooling fluid, as well as the walls of the internal circuit of the stack itself, were added. The coolant was taken as a non-compressible fluid. To describe the behaviour of the laminar flow, the incompressible fluid equations of Navier–Stokes were used [57], [58]. In (5), the vector formulation used to calculate the laminar flow of the refrigerant fluid is shown.

The incompressibility of the fluid, together with mass and moment conservation, yield the equations that describe the laminar flow of the refrigerant fluid:

$$\nabla \cdot u = 0, \tag{5}$$

$$\frac{\partial \rho}{\partial t} + \nabla \cdot (\rho u) = 0, \tag{6}$$

and

$$\rho \frac{\partial u}{\partial t} + \rho (u \cdot \nabla) u = \nabla \cdot [-pI + \tau] + F, \tag{7}$$

where ∇ is the fluid divergence, u is the fluid velocity vector [m/s], ρ is the fluid density [kg/m³], p is the fluid pressure [Pa], I is the identity matrix, F is the volume force vector [N/m³], and τ is the tensor of viscous tensions [Pa] given by

$$\tau = 2\mu S - \frac{2}{3}\mu(\nabla \cdot u)I, \tag{8}$$

where μ is the dynamic viscosity of the fluid [Pa·s] and S is the strain rate tensor given by

$$S = \frac{1}{2}(\nabla u + (\nabla u)^T). \tag{9}$$

The water flow rate and cross-sectional area of the cooling circuit inlet were obtained experimentally and were found to be 1.07 l/min and 104.275 mm², respectively. From these data, a fluid input velocity of 0.171 m/s was defined as the input boundary condition. For the output of the fluid, the pressure contour conditions were defined so that the reflux was zero at the output.

Figs. 10(a) and 10(b) show the flow lines through the cooling circuit and a cross-section on each bipolar plate of the magnitude of the fluid velocity along the cooling circuit, respectively.
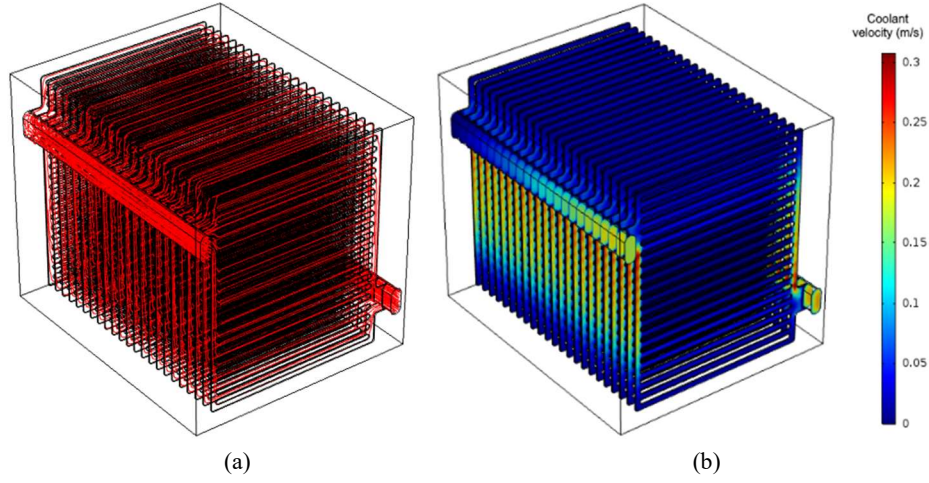
Fig. 10. (a) Flow lines and (b) velocity magnitude along the cooling circuit.

As can be seen in Fig. 10(a), the coolant flowed through all of the channels of the cooling circuit. Fig. 10(b) shows that the initial fluid velocity at the inlet of the cooling circuit duct was greater than at the end of the same duct. In addition, it can be seen that the fluid velocity was greater in the centre of the duct than near the walls, due to the hydraulic load losses of the fluid flowing through the conduct, which in turn depend on the dynamic viscosity of the coolant. As the cooling fluid entered the stack through the inlet conduit, the flow was diverted through the vertical distribution channels of each bipolar plate. The cross-sectional area of the main inlet duct was larger than those of the vertical distribution channels of the plates, so the fluid velocity increased through those channels. Subsequently, the fluid was distributed through the horizontal channels of each plate, increasing the effective cross-sectional area and decreasing the velocity of the fluid again. As the velocity of the fluid was reduced through the parallel channels of each plate, more heat could be absorbed from the stack. The opposite effect occurred at the outlet as the output vertical distribution channel of each plate collected the streams from the parallel channels, increasing the fluid velocity again.

To verify the initial hypothesis that the fluid regime was laminar, the Reynolds number Re was obtained as follows:

$$Re = \frac{u \cdot D_h}{v}, \tag{10}$$

where v is the kinematic viscosity of the fluid [m²/s] and D_h is the hydraulic diameter of the cooling circuit [m]:

$$v = \frac{\mu}{\rho} \tag{11}$$

and

$$D_h = \frac{4A}{P_w}, \tag{12}$$

where A is the cross-sectional area of the conduit [m²] and P_w is the wetting perimeter [m]. Since the circuit was non-circular and had different cross-sections, D_h and Re were determined for each section. In Fig. 11, the values of Re along the internal cooling circuit are shown.
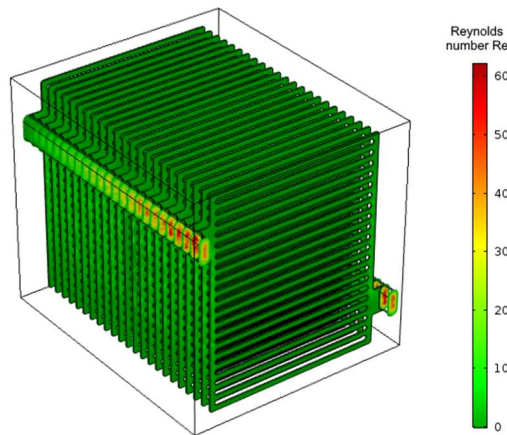

Fig. 11. Reynolds number along the cooling circuit.

As can be seen in Fig. 11, the maximum value of Re is 60.68. The ratio between the inertial and viscous forces is much lower than 2,300, validating the initial hypothesis that the flow was laminar rather than turbulent [59].

Once the physics of laminar flow had been validated, the physics of heat transfer in solids and fluids was implemented. Since internal energy is a rather difficult quantity to measure and use in simulations, the first law of thermodynamics rewritten in terms of temperature was used for the heat transfer simulation. In (13), the heat formulation resulting from various thermodynamic relationships is shown for the case of a fluid [60]:

$$\rho C_p \left(\frac{\partial T}{\partial t} + u \cdot \nabla T \right) + \nabla \cdot q = \alpha_p T \left(\frac{\partial p}{\partial t} + u \cdot \nabla p \right) + \tau : \nabla u + Q, \tag{13}$$

where C_p is the specific heat at constant pressure [J/(kg·K)], T is the absolute temperature [K], q is the heat flow by conduction [W/m^2], α_p is the thermal expansion coefficient [1/K], and Q represents the heat source [W/m^3]. The remaining variables are those already mentioned in (5)–(9). This equation assumes that mass is always conserved, which means that the density and velocity must be related through (6). The thermal expansion coefficient can be determined using

$$\alpha_p = -\frac{1}{\rho} \frac{\partial \rho}{\partial T}. \tag{14}$$

The heat transfer in the stack can be calculated using the Fourier conduction law, which establishes that the conductive heat flux q_i is proportional to the temperature gradient:

$$q_i = -k \frac{\partial T}{\partial x_i}, \tag{15}$$

where k is the thermal conductivity [W/(m·K)]. In a solid, the thermal conductivity can be anisotropic, i.e. it can have different values in different directions. Therefore, k becomes the tensor shown in (16) and the heat flow by conduction is given by (17):

$$k = \begin{bmatrix} k_{xx} & k_{xy} & k_{xz} \\ k_{yx} & k_{yy} & k_{yz} \\ k_{zx} & k_{zy} & k_{zz} \end{bmatrix} \tag{16}$$

and

$$q_i = -\sum_j k_{ij} \frac{\partial T}{\partial x_j} . \tag{17}$$

The first term of (13) represents the work performed due to pressure changes and is responsible for heating a fluid under adiabatic compression. It is generally negligible for flows with low Mach numbers [61]. The second term on the right-hand side of (13) represents the viscous dissipation of a fluid, where the operation ':' is a contraction and in this case can be written as

$$\tau : \nabla u = \sum_n \sum_m \tau_{nm} \nabla u_{nm}. \tag{18}$$

Introducing (17) into (13), rearranging the terms, and ignoring the viscous dissipation and working pressure, the equation for heat transfer equation in fluids can be obtained:

$$\rho C_p \frac{\partial T}{\partial t} + \rho C_p u \cdot \nabla T = \nabla \cdot (k \nabla T) + Q. \tag{19}$$

If the velocity field u is null, (20), which governs heat transfer by pure conduction in the solid state can be obtained:

$$\rho C_p \frac{\partial T}{\partial t} + \nabla \cdot (-k \nabla T) = Q + Q_{conv}. \tag{20}$$

Additionally, in (20), the term Q_{conv} has been introduced, which represents the natural convection losses due to the stack and ambient air temperature differences. The Newton–Richman equation that describes the losses by natural convection is

$$Q_{conv} = h \cdot A_s \cdot (T_s - T_a), \tag{21}$$

where h is the heat transfer coefficient [J/(s·m^2·K)], A_s is the surface area exposed to the environment [m^2], T_s is the stack surface temperature [K], and T_a is the ambient temperature [K]. h is given by

$$h = \frac{Nu \cdot k_a}{L}, \tag{22}$$

where Nu is the Nusselt number, k_a is the thermal conductivity of air [W/(m·K)], and L is the height of the stack sides exposed to the ambient air [m]. Nu for the case of external natural convection correlation in vertical plates is given by [60]

$$Nu = 0.825 + \frac{0.387 \cdot Ra^{1/6}}{\left(1 + \left(\frac{0.492}{Pr} \right)^{9/16} \right)^{8/27}}, \tag{23}$$

where Ra is the Rayleigh number and Pr is the Prandtl number, which are defined in (24) and (25), respectively:

$$Ra = \frac{g \cdot \alpha_p \cdot \rho^2 \cdot C_p \cdot |T_s - T_a| \cdot L^3}{k_a \cdot \mu} \quad (24)$$

and

$$Pr = \frac{C_p \cdot \mu}{k_a}, \quad (25)$$

where g is the acceleration of gravity [m/s^2]. The remaining variables are those defined in (7), (8), and (13) for the case of the air. All temperature-dependent variables are evaluated at the boundary layer temperature T_{bl} given by

$$T_{bl} = \frac{T_s - T_a}{2}. \quad (26)$$

To validate the physics of heat transfer in the stack and coolant, initial conditions of ambient air, stack and coolant temperatures of 293.15 K, and a temperature of 338.15 K on the left face of the stack were applied. Radiation cooling was neglected due to the small difference between the ambient temperature and stack surface temperature. Under these conditions, a 20 s transient simulation was performed. Figs. 12(a) and 12(b) depict the resulting temperature propagation through the stack and the cooling fluid without and with fluid movement, respectively.
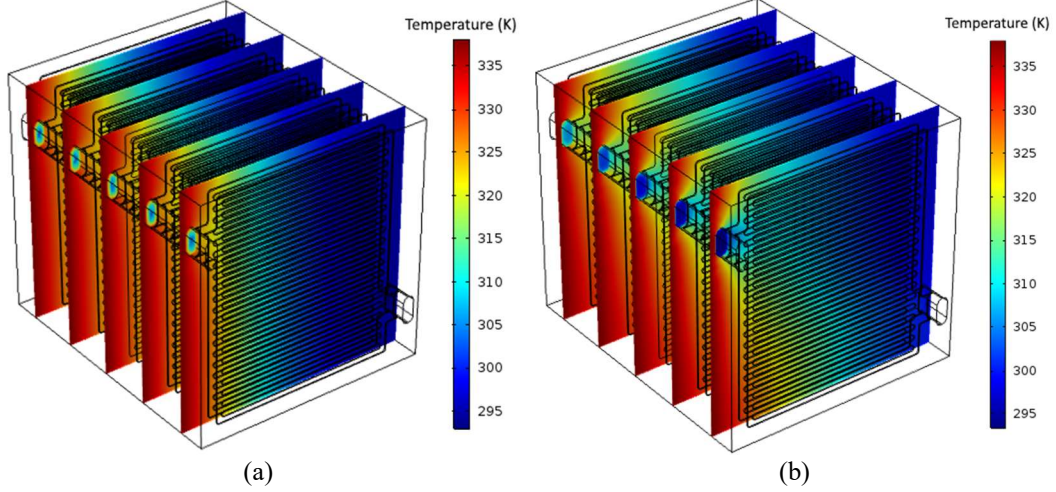

(a)   (b)

Fig. 12. Temperature propagation through the stack and coolant (a) without and (b) with fluid movement.

Fig. 12(a) shows how the heat propagated from the side to which the 338.15 K temperature was applied to the rest of the stack. Since the stack had a much higher thermal conductivity than the coolant, the heat propagated through the fluid more slowly than through the stack. Fig. 12(b) shows the results obtained by combining the physics of heat transfer in solids and fluids with the physics of laminar flow. It can be seen how the cooling fluid transported the heat it received from one side of the stack along the channels of the refrigeration circuit. In Section 4, the validation of the three types of physics with real data obtained from the laboratory tests with the PEMFC-based CHP system is described.

In Section 3.3, the coupling of the thermodynamic submodel with the ANN submodel presented in Section 3.1 is shown.

3.3.   Complete model configuration

The configuration of the model proposed in this report is based on the coupling of the ANN submodel described in Section 3.1 with the finite element method (FEM)-based submodel described in Section 3.2. Fig. 13 shows the structure of the proposed model.
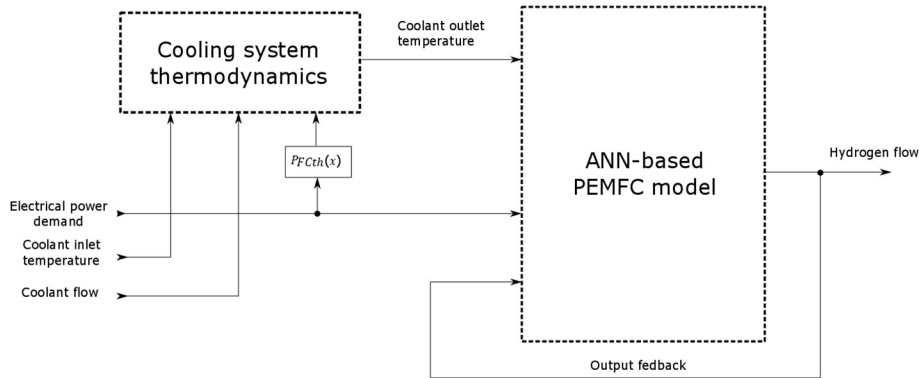

Fig. 13. Structure of the PEMFC-based CHP system model.

The block labelled "Cooling system thermodynamics" in Fig. 13 is intended to calculate the coolant outlet temperature as a function of the electrical power demand and the coolant flow rate and inlet temperature. The coolant outlet temperature and

electrical power demand are introduced into the ANN to obtain the hydrogen consumption rate. In this way, the model can predict the electrical and thermal efficiencies of the PEMFC-based CHP system over wide ranges of the input variables.

To establish the heat source Q as a function of the electrical power P_{FCel} demanded of the FC system, a fourth-degree polynomial was developed by using the data obtained in the laboratory tests. In (27), the polynomial adjustment that relates the thermal power P_{FCth} generated by the stack and the electrical power P_{FCel} demanded of the FC system is shown. The P_{FCth} value considers the thermal power recovered by the cooling system as well as the natural convection losses due to the temperature difference between the stack surface and ambient temperatures, assuming the latter to be 293.15 K. P_{FCel} values of less than 50 W are not taken into account to recover heat from the stack because the amount of heat that could be extracted is negligible.

$$\begin{cases} if\ P_{FCel} < 50 \rightarrow P_{FCth} \approx 0 \\ \quad if\ P_{FCel} \geq 50 \rightarrow P_{FCth}(x) = -0.5208 \cdot x^4 - 6.193 \cdot x^3 + 11.96 \cdot x^2 + 203.6 \cdot x + 361.6 \end{cases} \tag{27}$$

where x is the electrical power normalized according to (28). The sum squared error of the polynomial fit was determined to be 4.9275e-26.

$$x = \frac{P_{FCel} - 4\ 50}{158.1} \tag{28}$$

By using (29), Q corresponding to P_{FCth} calculated by employing (27) and (28) can be obtained:

$$Q = \frac{P_{FCth}}{V}, \tag{29}$$

where V is the FC stack volume [m³].

The new configuration can provide the coolant outlet temperature and hydrogen consumption rate as functions of the inlet temperature of the refrigerant fluid, electric power demand, and a wide range of coolant flow rates. However, obtaining the electrical and thermal efficiencies of the FC system through simulations with the proposed configuration involves high computational cost and could not be used to manage the system optimally in real time. To implement the complete model of the system in real time, a 3D lookup table (LUT) that provides the coolant outlet temperature as functions of the electrical power demand and the coolant inlet temperature and flow rate was built. A second 3D LUT was built with the same input parameters to provide the stack temperature instead of the coolant outlet temperature and thereby to obtain the minimum flow restriction curves to prevent the stack temperature from exceeding a predefined value.

To build the 3D LUT, a simulation was conducted based on the submodel presented in Section 3.2, in which parametric sweeps of the coolant flow rate, coolant inlet temperature, and electrical power demand were conducted, enabling rapid prediction of the cooling fluid temperature as functions of the three input variables in the 3D LUT. Table 3 shows the ranges of input variables of the thermodynamic submodel that were employed to perform the parametric sweeps to implement the 3D LUT.

Table 3. Ranges of the variables for the parametric sweeps.

Parameter	Units	Range	Step
Coolant inlet temperature	ºC	[16…60]	4
Coolant flow rate	l/min	[0…1.5]	0.1
Electrical power demand	W	[0…600]	100

Fig. 14 shows the coolant outlet temperature as functions of the coolant flow rate and inlet temperature for an electrical power demand of 600 W.
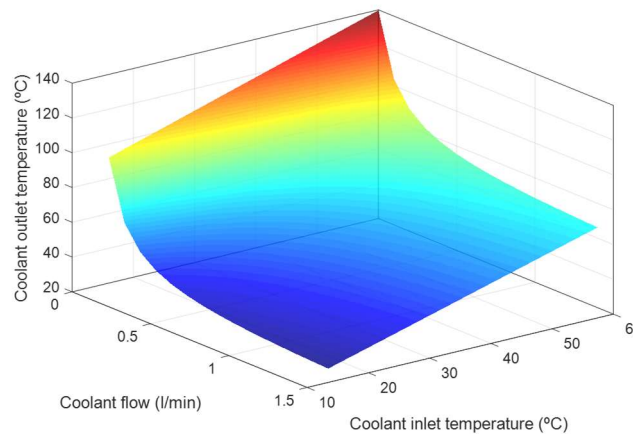

Fig. 14. Coolant outlet temperature simulated as functions of the coolant flow rate and inlet temperature (P_{FCel} = 600 W).

As can be seen in Fig. 14, the coolant outlet temperature increases as the coolant flow rate decreases and the coolant inlet temperature increases. The variation of the coolant outlet temperature as a function of the coolant inlet temperature can be approximated using a linear function. However, nonlinearity can be perceived between the coolant flow rate and coolant outlet temperature variations.

Figs. 15(a) and 15(b) show the coolant outlet temperature as a function of the coolant flow rate for various electrical power demands and coolant inlet temperatures of 16 °C and 60 °C, respectively.
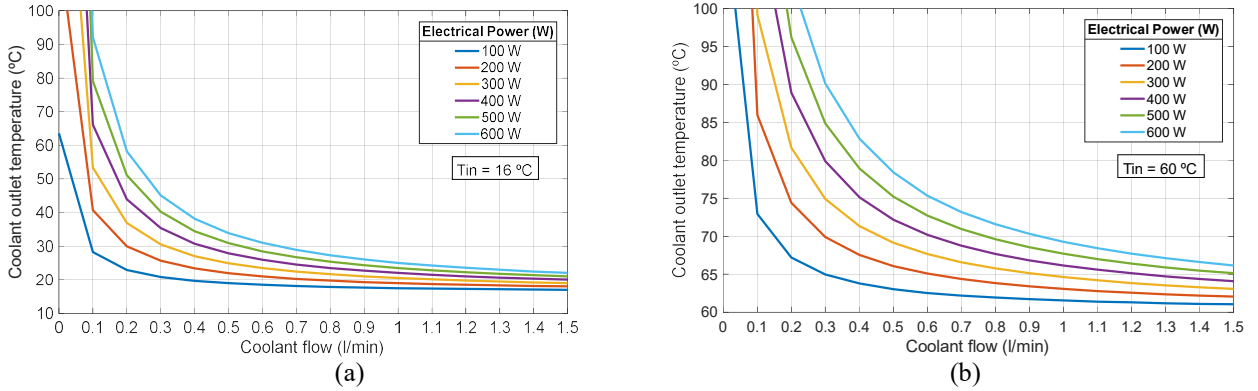

Fig. 15. Coolant outlet temperature as a function of the coolant flow rate for various electrical power demands and coolant inlet temperatures of (a) 16 ºC and (b) 60 ºC.

Fig. 15 shows the abovementioned nonlinear relationship between the coolant outlet temperature and flow rate as well as the nonlinearity between the coolant outlet temperature and electrical power demand. As the electrical power demand increases and the coolant flow rate decreases, the exponential curve of the coolant outlet temperature becomes more pronounced. This exponential behaviour implies that the cooling control system must restrict the minimum flow rate to be set for each electrical power demand and coolant inlet temperature so that the nominal operating temperature of the stack is not exceeded.

Figs. 16(a) and 16(b) show the coolant outlet temperature as a function of the electrical power demand for various coolant inlet temperatures and coolant flow rates of 0.05 l/min and 1 l/min, respectively.
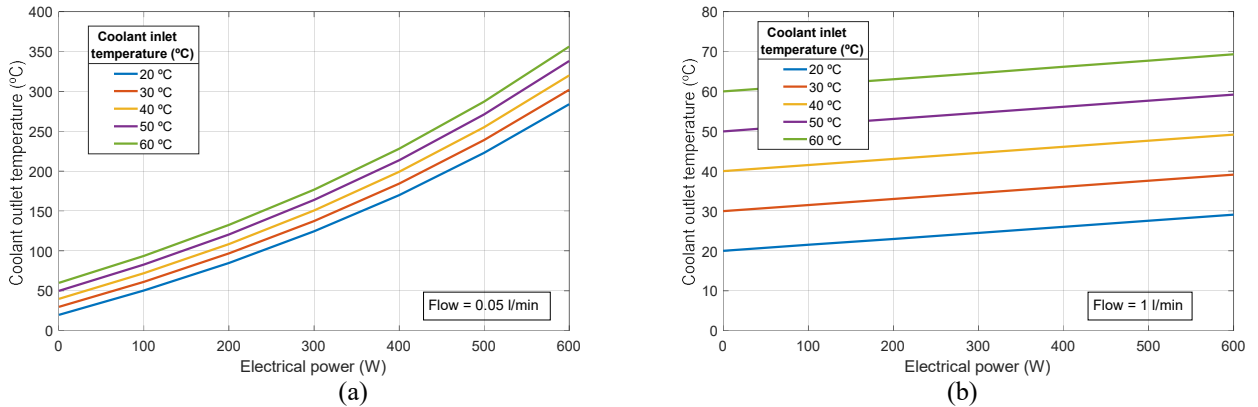

Fig. 16. Coolant outlet temperature as a function of the electrical power demand for various coolant inlet temperatures and coolant flow rates of (a) 0.05 l/min and (b) 1 l/min.

By comparing Figs. 16(a) and 16(b), it can be seen that the nonlinearity between the coolant outlet temperature and electrical power demand is present only for low coolant flow rates, while this relationship can be approximated using a linear function for high flow rates.

Due to the two existing nonlinearities, to minimize the error involved in obtaining the intermediate solutions, it is necessary to perform interpolations that respect the monotonicity of the data and preserve the shapes of curves of the coolant outlet temperature as functions of the electric power demand and coolant flow rate. In this case, 3D interpolation was implemented using linear interpolation to obtain the coolant outlet temperature as a function of the inlet temperature and piecewise cubic Hermite interpolating polynomial (PCHIP) interpolation to obtain the coolant outlet temperature as functions of the coolant flow rate and electrical power demand. Equation (30) shows the PCHIP interpolation polynomial used [62]:

$$y(x) = h_{00}(t)y_k + h_{10}(t)(x_{k+1} - x_k)m_k + h_{01}(t)y_{k+1} + h_{11}(t)(x_{k+1} - x_k)m_{k+1} \quad for \quad k = 1, \ldots, n, \tag{30}$$

where x is the discrete value entered; $y(x)$ is the interpolated value; x_k and x_{k+1} are the values before and after x, respectively; y_k and y_{k+1} are the values before and after $y(x)$, respectively; m_k and m_{k+1} are the tangents evaluated at points k and $k + 1$, respectively; $h_{ii}()$ are the basic Hermite functions; and t is the point at which each $h_{ii}()$ is evaluated. t and m_k were respectively determined using

$$t = \frac{x - x_k}{x_{k+1} - x_k} \tag{31}$$

and

$$m_k = \frac{\Delta_{k-1} + \Delta_k}{2}, \tag{32}$$

where Δ_{k-1} and Δ_k are the slopes of the secant lines between successive points, which can be obtained using

$$\Delta_k = \frac{y_{k+1} - y_k}{x_{k+1} - x_k}. \tag{33}$$

The basic Hermite functions $h_{ii}(t)$ are

$$h_{00}(t) = B_0(t) + B_1(t), \tag{34}$$

$$h_{10}(t) = \frac{1}{3} B_1(t), \tag{35}$$

$$h_{01}(t) = B_3(t) + B_2(t), \tag{36}$$

and

$$h_{11}(t) = B_0(t) + B_1(t), \tag{37}$$

where B_i are the elements of the Bernstein polynomials of order 3 used to compose $h_{ii}()$ and are given by

$$B_i(t) = \binom{3}{i} \cdot t^i \cdot (1 - t)^{3-i}. \tag{38}$$

The 3D LUT calculates the parameters of the PCHIP interpolation polynomials that fit the necessary curves for interpolation. Specifically, a dynamic interpolation algorithm recalculates the coefficients of the PCHIP polynomials as functions of the value to be interpolated.

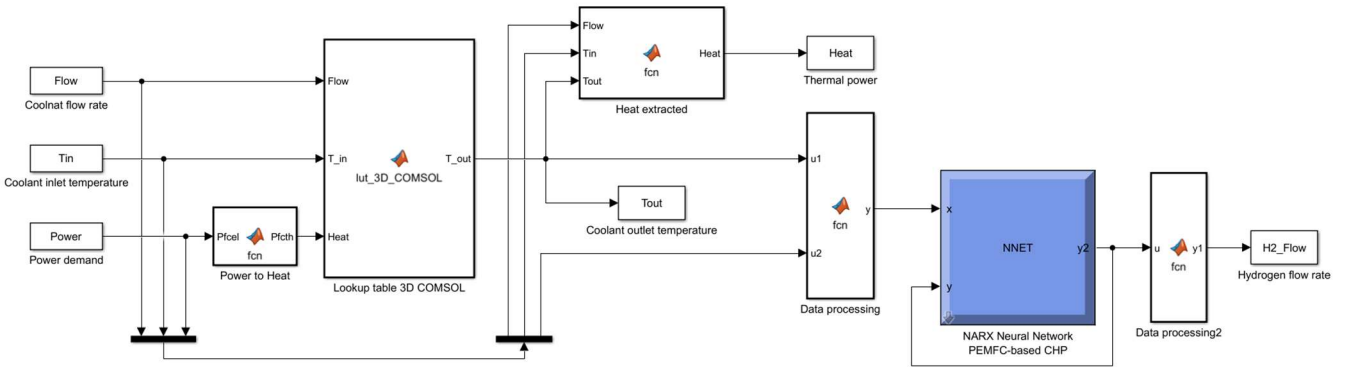Fig. 17 shows the implementation of the proposed model in the MATLAB/Simulink environment.

Fig. 17. Configuration of the PEMFC-based CHP system model in the MATLAB/Simulink environment.

Section 4 describes the validation of the proposed model, the verification of the effectiveness of the implemented 3D interpolation, depicts the flow restriction as functions of the coolant inlet temperature and electric power demand, and presents the simulation results obtained using the model.

4. Results and discussion

To validate the thermodynamic behaviour of the FC cooling system, a simulation of the stack-cooling circuit assembly with real conditions extracted during experimentation with the HP600 at nominal power was performed. During the simulation, the inlet and outlet temperatures of the coolant fluid and coolant flow rate were recorded. To obtain the losses due to natural convection, a thermographic image of the surface exposed to the environment was taken and the ambient temperature during the test was measured. Fig. 18 shows the thermographic image of the stack during the test, which illustrates that the stack was thermally insulated on several faces. Thus, the heat loss due to natural convection was very low.
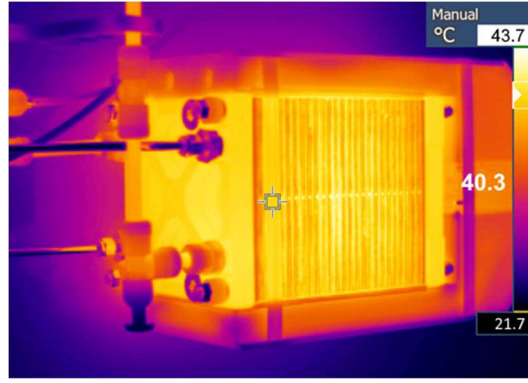
Fig. 18. Thermographic image of the stack during the test at nominal electrical power.

Table 4 lists the values obtained during the test at the rated electrical power (600 W), after the stack temperature had stabilised.

Table 4. Values obtained during the test at nominal power.

Parameter	Value
Coolant inlet temperature	31.5 ºC
Coolant outlet temperature	38.97 ºC
Stack surface temperature	40.3 ºC
Ambient temperature	20 ºC
Coolant mass flow	0.01783 kg·s⁻¹
Natural convection losses	2.32 W
Recovered thermal power	557.64 W

Next, a permanent regime simulation for the input values in Table 3 was performed. The heat source was defined as the sum of the recovered thermal power and natural convection losses. Figs. 19(a) and 19(b) show the temperature distributions in the stack and cooling circuit obtained from the simulation.
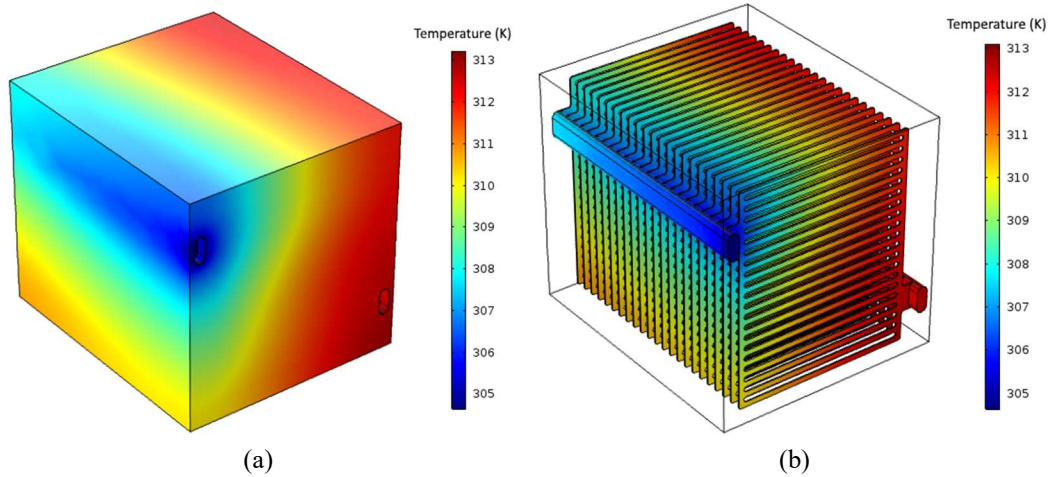

(a)   (b)

Fig. 19. Temperature distributions in the (a) stack and (b) cooling circuit.

As can be seen in Fig. 19, the simulation results accurately approximate the behaviour obtained experimentally. The average temperature of coolant outlet obtained from the simulation was found to be 39.22 °C. Thus, absolute and relative errors of 0.25 °C and 0.64%, respectively, were obtained. Equation (39) was used to quantify the thermal power extracted by the coolant from the stack:

$$P_{th} = C_p \cdot \dot{m} \cdot (T_{out} - T_{in}), \tag{39}$$

where C_p is the heat capacity of the coolant at constant pressure [J·(kg·K)], $\dot{m}$ is the mass flow of the coolant [kg/s], and T_{out} and T_{in} are the coolant outlet and inlet temperatures [K], respectively.

The thermal power extracted from the stack obtained from the simulation was 576.3 W, yielding an absolute error of 18.67 W and a relative error of 3.35% compared to the experimentally obtained data. After performing several simulations at different powers, it was verified that the maximum errors were obtained for the case in which the stack produced the nominal power. Thus, it was concluded that the thermodynamic model can obtain the coolant outlet temperature as functions of the electrical power demand and coolant inlet temperature and flow rate with high precision. In addition to providing the coolant outlet temperature, the FEM-based thermodynamic model facilitates analysis of the temperature distribution through the stack to detect hot spots and limit the flow of the refrigerant to a certain value.

To verify the effectiveness of the 3D interpolation, a simulation was conducted using a coolant inlet temperature, a coolant flow rate, and an electric power demand different from those employed when performing the parametric sweeps. Specifically, a coolant flow rate of 0.15 l/min, a coolant inlet temperature of 18 °C, and an electrical power demand of 550 W were utilized. Fig. 20 shows the operating point obtained from the simulation, as well as the two operating points and two coolant outlet temperature curves obtained by implementing linear and PCHIP interpolation.
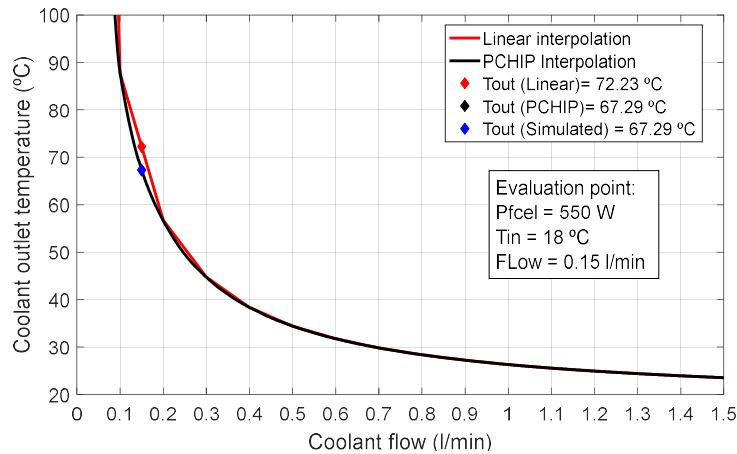

Fig. 20. Coolant outlet temperature obtained as a function of the coolant flow rate by implementing linear and PCHIP interpolation.

Linear interpolation yielded an output temperature of 72.23 °C, while PCHIP interpolation produced a temperature of 67.29 °C. The absolute and relative errors obtained by linear interpolation relative to the value obtained by simulation were found to be 4.94 ºC and 7.34%, respectively. For the PCHIP interpolation, the errors were null.

The maximum relative error of the coolant outlet temperature obtained by linear interpolation was 24.75% for a coolant flow rate of 0.05 l/min, an inlet temperature of 60 °C, and an electrical power demand of 600 W. However, this error was obtained at a theoretical operating point that could not be achieved in a real situation, since the stack temperature for those input values would reach 285.51 ºC. The errors obtained at all operating points checked by simulation were null in the case of PCHIP interpolation.

Although the model considers all operating points as functions of the electrical power demand, coolant flow rate, and inlet temperature, in order not to degrade the PEMFC due to overheating it is essential to obtain the flow restriction curves as functions of the input variables. In a real system, the stack temperature could be controlled by closed-loop control with feedback of the stack temperature. Thus, by acting on the flow rate of the cooling fluid and/or dissipating the heat via a heat exchanger in case it is not used, the stack temperature could be adjusted to the desired value. However, due to the thermal inertia of the system, if a precise model is not available, the control system would not be able to predict the optimum coolant flow rate without risking exceeding the temperature set point. With the proposed model, the cooling circuit control system can anticipate the optimum flow rate that maximizes the efficiency of the PEMFC, depending on the variables that influence the stack temperature, such as the coolant inlet temperature and heat generated by the exothermic reactions.

To establish the limits within which the flow rate can be varied, a stack temperature limit of 65 ºC was established. Taking into account this restriction, the curves of the minimum coolant flow rate as functions of the coolant inlet temperature and electrical power demand were obtained. Fig. 21 shows the cut of the 65 °C plane with the stack temperature surface for an electrical power demand of 600 W.
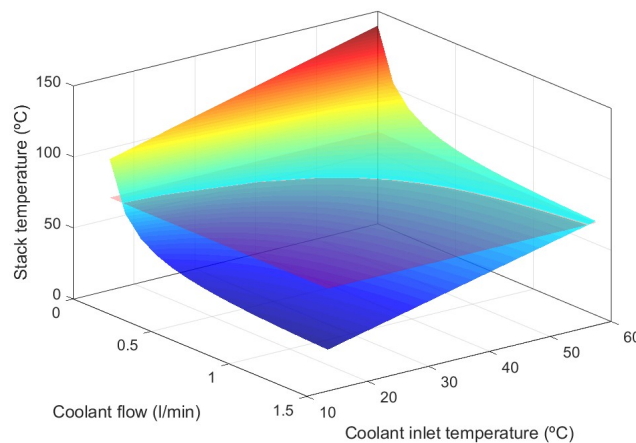

Fig. 21. 65 ºC temperature plane cut with the stack temperature surface (P_{FCel} = 600 W).

The restriction curves were obtained by performing a sweep over the 3D LUT containing the stack temperature as functions of the coolant inlet temperature, flow rate, and electrical power demand. To obtain intermediate solutions, the 3D interpolation described above was used. When applying an optimization strategy, the control algorithm could access the 3D LUT to obtain the minimum coolant flow restrictions for any real operating point.

Fig. 22 shows the coolant minimum flow rate as a function of the coolant inlet temperature for several electrical power demands.
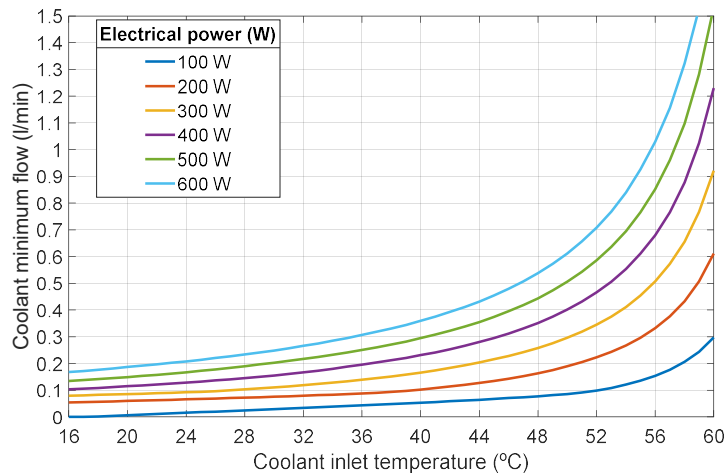

Fig. 22. Restriction curves of the coolant flow rate as a function of the coolant inlet temperature for various electrical power demands.

As can be seen in Fig. 22, as the coolant inlet temperature increases linearly, the minimum coolant flow rate to be set increases exponentially. To maintain a stack temperature below 65 °C, it would be necessary to increase the flow rate to more than 1.5 l/min for coolant inlet temperatures greater than 60 °C and electrical power demands greater than 500 W. However, the maximum thermal power extracted from the stack remains essentially constant from a certain coolant flow rate, which depends mainly on the electrical power demand. Fig. 23 shows the maximum thermal power extracted from the stack as a function of the coolant flow rate, for a coolant inlet temperature of 20 °C and several electrical power demands.
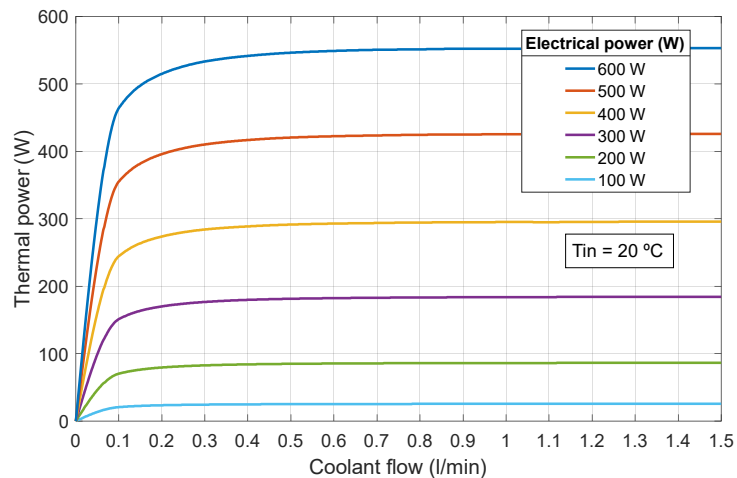

Fig. 23. Maximum thermal power extracted as a function of the coolant flow rate for a coolant inlet temperature of 20 °C and various electrical power demands.

To validate the complete model and check the effect of the coolant flow rate regulation on the electrical and thermal efficiencies of the PEMFC, a simulation was performed using the proposed model and the data obtained in the laboratory tests. Specifically, real data obtained for a flow rate of 1 l/min were compared with simulation data obtained for flow rates of 0.3281 l/min and 1 l/min. It should be noted that a flow rate of 0.328 l/min was obtained from the minimum flow restriction curves, so the stack temperature did not exceed 65 °C. Under these conditions, the output values of the coolant outlet temperature and hydrogen flow rate were recorded. With these values, the thermal powers extracted as well as the electrical and thermal efficiencies of the system were calculated. Fig. 24(a) shows the coolant inlet and outlet temperatures for a coolant flow rate of 1 l/min (real and simulated) and 0.328 l/min (simulated), while Fig. 24(b) depicts the electrical power demand and thermal power extracted from the stack for both coolant flow rates.
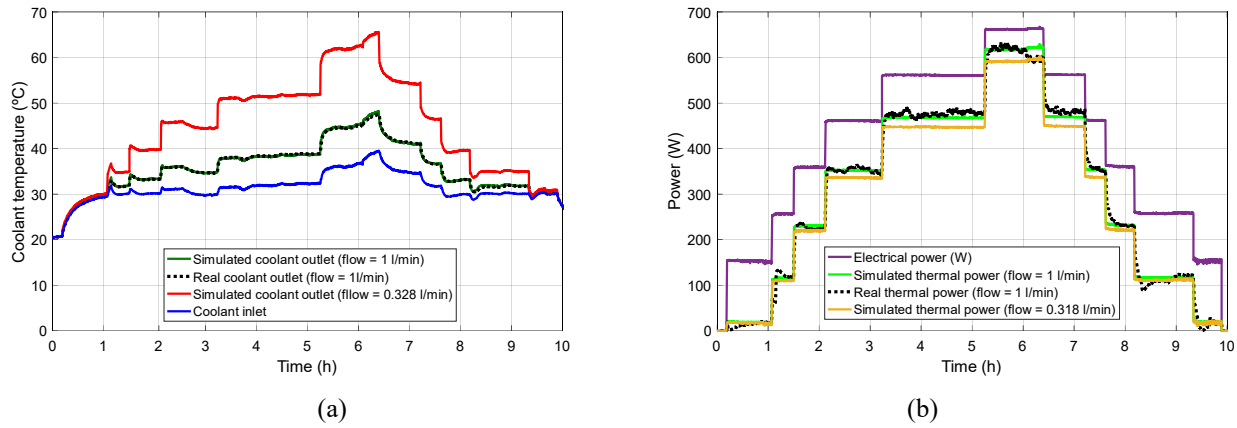
Fig. 24. (a) Coolant inlet and outlet temperatures and (b) electrical power demand and thermal power extracted for the real and simulated coolant flow rates.

Fig. 24(a) shows that, for the same coolant inlet temperature, reducing the flow rate by 67.2% compared to the real case increases the coolant outlet temperature by 36.55% (from 47.6 °C to 65 °C). Fig. 24(b) shows that, although the temperature for the lower flow rate case is higher, the thermal power extracted from the stack is not greater than that obtained in the real case in which the flow rate was 1 l/min. The maximum thermal power is reduced by 4.68% (from 633.1 W to 603.48 W), because the coolant flow rate decreases enough to cause the extracted thermal power to be lower, resulting in a stack temperature increase. An increase in stack temperature positively influences the electrical efficiency of a PEMFC, since at higher temperatures the catalytic reactions are favoured in the electrochemical conversion process.

Fig. 25 shows the hydrogen flow rate, as well as the thermal and electrical efficiencies of the system, for the real and simulated cases used to obtain Fig. 24.
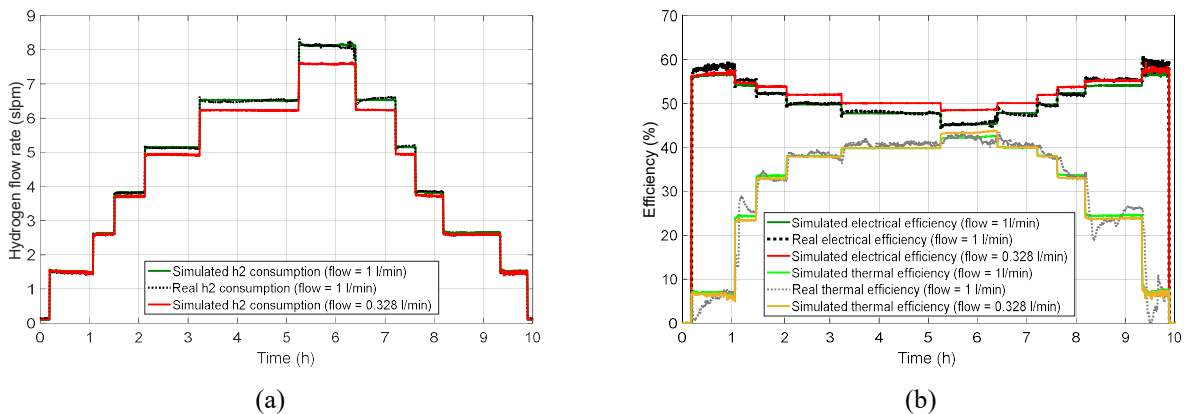

Fig. 25. (a) Hydrogen flow rate and (b) thermal and electrical efficiencies for the real and simulated coolant flow rates.

As can be seen in Fig. 25(a), for the simulated case with a coolant flow rate of 0.328 l/min, the hydrogen consumption decreases with increasing stack temperature. In the best case, the hydrogen consumption is reduced by 8.17% (from 8.32 slpm to 7.64 slpm). Fig. 25(b) shows that the hydrogen consumption reduction implies an increase of the electrical efficiency of the PEMFC. In the best case, the electrical efficiency is increased by 3.67% (from 44.68% to 48.35%). Meanwhile, at low coolant outlet temperatures, the thermal efficiency is slightly lower for the case with a flow rate of 0.328 l/min. However, as the electrical power demand increases, and therefore the operating temperature increases, the thermal efficiency increases slightly, because the effect of the thermal power reduction is compensated for by hydrogen consumption reduction. Fig. 26 shows the global efficiency curves for the real and simulated cases.
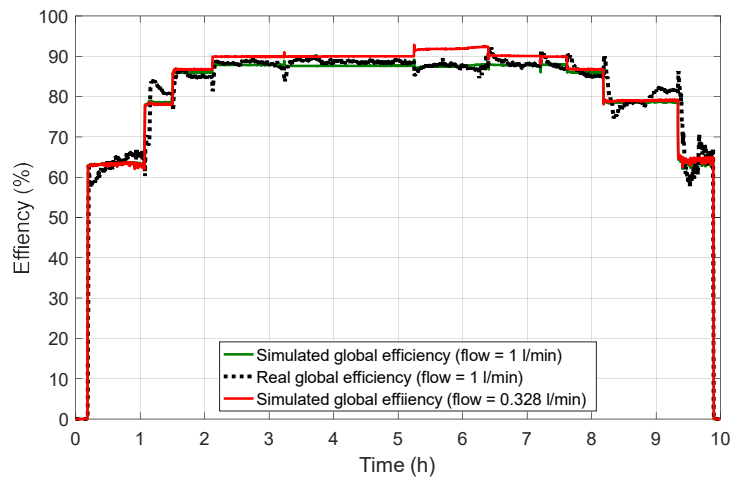
Fig. 26. Global efficiency for the real and simulated coolant flow rate cases.

As can be seen in Fig. 26, the overall efficiency obtained for the optimum flow rate case is higher across nearly the entire simulated range. The maximum overall efficiency is 91.8%, and the real overall efficiency at that point is 87.82%.

The maximum absolute and relative errors were determined to be 0.25 °C and 0.64%, respectively, when simulating the coolant outlet temperature using a flow rate of 1 l/min and 0.12 slpm and 1.44%, respectively, when simulating the hydrogen flow rate using a flow rate of 1 l/min. In general, the error of the hydrogen flow rate increases as the load factors decrease and decreases as the FC load factor increases. In addition, the absolute error for the simulated electrical efficiency was found to be negative for low load factors, implying that the simulated electrical efficiency obtained using a flow rate of 0.328 l/min could be higher in a real case.

Due to the lack of real data for a flow rate of 0.328 l/min, it was not possible to compare the simulation results with experimental results in that case. However, the absolute and relative maximum errors obtained with the thermodynamic model were verified to be 0.25 ºC and 0.64%, respectively, when simulating the coolant outlet temperature and 18.67 W and 3.35%, respectively, when simulating the thermal power extracted from the stack.

The results presented indicate that the proposed model can accurately predict the electrical and thermal efficiencies of the system as functions of the coolant flow rate and outlet temperature and the electrical power demand. In a real situation in which only electric energy is demanded, the model can predict the optimum cooling fluid rate that maximizes the electrical efficiency of the system. In addition, compared to temperature control systems that use heat exchanger systems to release excess heat into the environment, the consumption required for temperature regulation can be minimized, since reducing the flow rate also reduces the energy required to operate the cooling pump.

For cases in which the energy demand is electrical and thermal, the model can predict the electrical and thermal efficiencies of the PEMFC over wide ranges of input variables. Thus, by using a control algorithm, it would be possible to establish the optimum operating point of the PEMFC that minimizes the total cost of the system. The control algorithm would try to obtain the optimum set point of the electric power to be produced and the coolant flow rate that minimizes the total cost of the system as functions of the electricity price, cost of obtaining hydrogen, maintenance costs, etc.

To obtain a single coolant output temperature and hydrogen consumption data for a given coolant flow rate, electrical power, and input temperature, the FEM-based model requires 1.5 h for simulation with a seventh-generation i7 processor at 3.9 GHz, a solid-state drive, and 32 GB of DDR4 RAM. Although accurate results can be obtained, this simulation time makes it impossible to use the model to develop strategies in real time. With the innovative modelling methodology proposed in this report, each operating point can be obtained in a maximum of 150 ms; that is, the simulation time could be decreased by 36,000 times without losing the resolution provided by an analytical–mechanistic model. This aspect allows for integration of the developed model into any embedded system with low hardware requirements, so that it can be executed in real time and, by means of a predictive control algorithm, the coolant flow and electric power set points to be applied to the PEMFC-CHP can be obtained.

Although the presented control algorithm does not optimize the total cost of the system, it is proposed as future research work to develop an algorithm that will take into account the total cost of the system to calculate the electric power set point to be produced and the optimum cooling flow rate that minimizes the generating cost of the system. In addition, it is proposed to include the consumption of the cooling pump in the model. In this regard, the optimization algorithm to be developed will have to include the refrigerant pump consumption as a variable to obtain the optimum operating point of the system.

Fig. 27 shows a possible real case in which the proposed model could be employed to develop new optimization strategies.
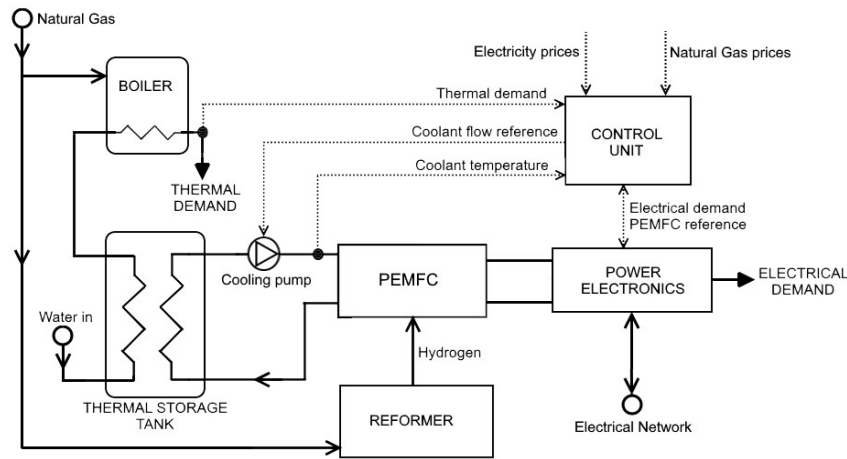
Fig. 27. Proposed scheme for optimizing a PEMFC-based CHP system.

Fig. 27 shows a PEMFC-based cogeneration system connected to the electricity grid and integrated with an auxiliary gas boiler and a thermal storage tank. Assuming that the hydrogen consumed by the PEMFC comes from a natural gas reformer, the control unit would have to establish the optimum operating point of the PEMFC system based on electricity and natural gas prices. Thus, the control unit would be based on an optimal control algorithm that would use the proposed model to calculate the cooling fluid flow and electric power to be produced, depending on the electrical demand, thermal demand, generating cost of the auxiliary boiler, and sale and purchase prices of electricity and natural gas. This calculation would be possible because the model presented can predict the electrical and thermal efficiencies of a PEMFC as functions of the abovementioned control instructions with high accuracy and in real time.

5. Conclusions

This paper has presented a model for the optimum management of the cooling system of a PEMFC-based CHP system. The model can be employed to obtain the hydrogen consumption rate and coolant outlet temperature as functions of the coolant inlet temperature and flow rate and the electrical power demand. Based on the calculated variables, the model can accurately predict the electrical and thermal efficiencies of the system over wide ranges of the input variables. The configuration of the proposed model is based on the combination of a finite element method-based thermodynamic submodel with an ANN-based submodel, using a 3D LUT and 3D interpolation algorithm.

The proposed modelling technique enabled a black-box model to be obtained from a white-box model without losing resolution. In addition, it facilitated reduction of the simulation time by a factor of 36,000 with respect to that of an analytical–mechanistic model, making it possible to use the model in real-time applications in which the energy demand varies quickly.

In addition, the fact that the developed model accounts for the effects of cooling flow regulation on the efficiency of the system provides an additional degree of freedom when developing controls intended for optimal management of PEMFC-based CHP systems.

Finally, this paper described the methodology used to develop the proposed model in depth, so that it can be employed to generate other PEMFC models for use in developing new optimization strategies.

Acknowledgment

References

[1] H. I. Onovwiona and V. I. Ugursal. Residential cogeneration systems: Review of the current technology. *Renewable and Sustainable Energy Reviews 10(5),* pp. 389-431. 2006. . DOI: http://dx.doi.org/10.1016/j.rser.2004.07.005.

[2] M. M. Maghanki, B. Ghobadian, G. Najafi and R.J. Galogah. Micro combined heat and power (MCHP) technologies and applications. *Renewable and Sustainable Energy Reviews 28*pp. 510-524. 2013. . DOI: http://dx.doi.org/10.1016/j.rser.2013.07.053.

[3] S. Murugan and B. Horák. A review of micro combined heat and power systems for residential applications. *Renewable and Sustainable Energy Reviews 64*pp. 144-162. 2016. . DOI: http://dx.doi.org/10.1016/j.rser.2016.04.064.

[4] H. R. Ellamla, I. Staffell, P. Brujlo, B.G. Pollet and S. Pasupathi. Current status of fuel cell based combined heat and power systems for residential sector. *J. Power Sources 293*pp. 312-328. 2015. . DOI: http://dx.doi.org/10.1016/j.jpowsour.2015.05.050.

[5] T. Elmer, M. Worall, S.Wu and S.B. Riffat. Fuel cell technology for domestic built environment applications: State of-the-art review. *Renewable and Sustainable Energy Reviews 42*pp. 913-931. 2015. . DOI: http://dx.doi.org/10.1016/j.rser.2014.10.080.

[6] P. E. Dodds, I. Staffell, A.D. Hawkes, F. Li, P. Grünewald, W. McDowall and P. Ekins. Hydrogen and fuel cell technologies for heating: A review. *Int J Hydrogen Energy 40(5),* pp. 2065-2083. 2015. . DOI: http://dx.doi.org/10.1016/j.ijhydene.2014.11.059.

[7] Y. Wang, K.S. Chen, J. Mishler, S.C. Cho and X.C. Adroher. A review of polymer electrolyte membrane fuel cells: Technology, applications, and needs on fundamental research. *Appl. Energy 88(4),* pp. 981-1007. 2011. . DOI: http://dx.doi.org/10.1016/j.apenergy.2010.09.030.

[8] E. S. Barbieri, P. R. Spina and M. Venturini. Analysis of innovative micro-CHP systems to meet household energy demands. *Appl. Energy 97*pp. 723-733. 2012. . DOI: http://dx.doi.org/10.1016/j.apenergy.2011.11.081.

[9] G. M. Kopanos, M. C. Georgiadis and E. N. Pistikopoulos. Energy production planning of a network of micro combined heat and power generators. *Appl. Energy 102*pp. 1522-1534. 2013. . DOI: http://dx.doi.org/10.1016/j.apenergy.2012.09.015.

[10] P. Ahmadi, I. Dincer and M. A. Rosen. Thermodynamic modeling and multi-objective evolutionary-based optimization of a new multigeneration energy system. *Energy Conversion and Management 76*pp. 282-300. 2013. . DOI: http://dx.doi.org/10.1016/j.enconman.2013.07.049.

[11] G. Angrisani, M. Canelli, A. Rosato, C. Roseli, M. Sasso and S. Sibilio. Load sharing with a local thermal network fed by a microcogenerator: Thermo-economic optimization by means of dynamic simulations. *Appl. Therm. Eng. 71(2),* pp. 628-635. 2014. . DOI: http://dx.doi.org/10.1016/j.applthermaleng.2013.09.055.

[12] P. Ghadimi, S. Kara and B. Kornfeld. The optimal selection of on-site CHP systems through integrated sizing and operational strategy. *Appl. Energy 126*pp. 38-46. 2014. . DOI: http://dx.doi.org/10.1016/j.apenergy.2014.03.085.

[13] A. D. Smith and P. J. Mago. Effects of load-following operational methods on combined heat and power system efficiency. *Appl. Energy 115*pp. 337-351. 2014. . DOI: http://dx.doi.org/10.1016/j.apenergy.2013.10.063.

[14] L. F. Fuentes-Cortés, J.M. Ponce-Ortega, F. Nápoles-Rivera, M. Serna-González and M.M. El-Halwagi. Optimal design of integrated CHP systems for housing complexes. *Energy Conversion and Management 99*pp. 252-263. 2015. . DOI: http://dx.doi.org/10.1016/j.enconman.2015.04.036.

[15] A. Alahäivälä, T. Heß, S. Cao and M. Lehtonen. Analyzing the optimal coordination of a residential micro-CHP system with a power sink. *Appl. Energy 149*pp. 326-337. 2015. . DOI: http://dx.doi.org/10.1016/j.apenergy.2015.03.116.

[16] E. Merkel, R. McKenna and W. Fichtner. Optimisation of the capacity and the dispatch of decentralised micro-CHP systems: A case study for the UK. *Appl. Energy 140*pp. 120-134. 2015. . DOI: http://dx.doi.org/10.1016/j.apenergy.2014.11.036.

[17] Z. Tian, J. Niu, Y. Lu, S. He and X. Tian. The improvement of a simulation model for a distributed CCHP system and its influence on optimal operation cost and strategy. *Appl. Energy 165*pp. 430-444. 2016. . DOI: http://dx.doi.org/10.1016/j.apenergy.2015.11.086.

[18] L. Mongibello, N. Bianco, M. Caliano and G. Graditi. Comparison between two different operation strategies for a heat-driven residential natural gas-fired CHP system: Heat dumping vs. load partialization. *Appl. Energy 184*pp. 55-67. 2016. . DOI: http://dx.doi.org/10.1016/j.apenergy.2016.09.106.

[19] T. Fang and R. Lahdelma. Optimization of combined heat and power production with heat storage based on sliding time window method. *Appl. Energy 162*pp. 723-732. 2016. . DOI: http://dx.doi.org/10.1016/j.apenergy.2015.10.135.

[20] M. Caliano, N. Bianco, G. Graditi and L. Mongibello. Economic optimization of a residential micro-CHP system considering different operation strategies. *Appl. Therm. Eng. 101*pp. 592-600. 2016. . DOI: http://dx.doi.org/10.1016/j.applthermaleng.2015.11.024.

[21] W. C. Long, R. Luck and P. J. Mago. Uncertainty based operating strategy selection in combined heat and power systems. *Appl. Therm. Eng. 98*pp. 1013-1024. 2016. . DOI: http://dx.doi.org/10.1016/j.applthermaleng.2015.12.131.

[22] Y. Devrim and A. Albostan. Enhancement of PEM fuel cell performance at higher temperatures and lower humidities by high performance membrane electrode assembly based on nafion/zeolite membrane. *Int J Hydrogen Energy 40(44),* pp. 15328-15335. 2015. . DOI: http://dx.doi.org/10.1016/j.ijhydene.2015.02.078.

[23] R. A. Silva, T. Hashimoto, G.E. Thompson and C.M. Rangel. Characterization of MEA degradation for an open air cathode PEM fuel cell. *Int J Hydrogen Energy 37(8),* pp. 7299-7308. 2012. . DOI: http://dx.doi.org/10.1016/j.ijhydene.2011.12.110.

[24] S. G. Kandlikar and Z. Lu. Thermal management issues in a PEMFC stack – A brief review of current status. *Appl. Therm. Eng. 29(7),* pp. 1276-1280. 2009. . DOI: http://dx.doi.org/10.1016/j.applthermaleng.2008.05.009.

[25] T. Jahnke, G. Futter, A. Latz, T. Malkow, G. Papakonstantinou, G. Tsotridis, P. Schott, M. Gérard, M. Quinaud, M. Quiroga, A.A. Franco, K. Malek, F. Calle-Vallejo, R. Ferreira de Morais, T. Kerber, P. Sautet, D. Loffreda, S. Strahl, M. Serra, P. Polverino, C. Pianese, et al. Performance and degradation of proton exchange membrane fuel cells: State of the art in modeling from atomistic to system scale. *J. Power Sources 304*pp. 207-233. 2016. . DOI: http://dx.doi.org/10.1016/j.jpowsour.2015.11.041.

[26] T. Ous and C. Arcoumanis. Degradation aspects of water formation and transport in proton exchange membrane fuel cell: A review. *J. Power Sources 240*pp. 558-582. 2013. . DOI: http://dx.doi.org/10.1016/j.jpowsour.2013.04.044.

[27] D. E. Curtin, R.D. Lousenberg, T.J. Henry, P.C. Tangeman and M.E. Tisak. Advanced materials for improved PEMFC performance and life. *J. Power Sources 131(1–2),* pp. 41-48. 2004. . DOI: http://dx.doi.org/10.1016/j.jpowsour.2004.01.023.

[28] G. Zhang and S. G. Kandlikar. A critical review of cooling techniques in proton exchange membrane fuel cell stacks. *Int J Hydrogen Energy 37(3),* pp. 2412-2429. 2012. . DOI: http://dx.doi.org/10.1016/j.ijhydene.2011.11.010.

[29] A. Faghri and Z. Guo. Challenges and opportunities of thermal management issues related to fuel cell technology and modeling. *Int. J. Heat Mass Transfer 48(19–20),* pp. 3891-3920. 2005. . DOI: http://dx.doi.org/10.1016/j.ijheatmasstransfer.2005.04.014.

[30] O. A. Shaneb and P. C. Taylor. Evaluation of alternative operating strategies for residential micro combined heat and power. Presented at 2010 IEEE International Energy Conference. 2010, . DOI: 10.1109/ENERGYCON.2010.5771664.

[31] A. Azmy and I. Erlich. Online optimal management of PEM fuel cells using neural networks. Presented at IEEE Power Engineering Society General Meeting, 2005. 2005, . DOI: 10.1109/PES.2005.1489132.

[32] H. Aki. S. Yamamoto, Y. Ishikawa, J. Kondoh, T. Maeda, H. Yamaguchi, A. Murata and I. Ishii. Operational strategies of networked fuel cells in residential homes. *IEEE Transactions on Power Systems 21(3),* pp. 1405-1414. 2006. . DOI: 10.1109/TPWRS.2006.879270.

[33] M. Y. El-Sharkh, M. Tanrioven, A. Rahman and M.S. Alam. Cost related sensitivity analysis for optimal operation of a grid-parallel PEM fuel cell power plant. *J. Power Sources 161(2),* pp. 1198-1207. 2006. . DOI: http://dx.doi.org/10.1016/j.jpowsour.2006.06.046.

[34] L. Barelli, G. Bidini, F. Gallorini and A. Ottaviano. An energetic–exergetic analysis of a residential CHP system based on PEM fuel cell. *Appl. Energy 88(12),* pp. 4334-4342. 2011. . DOI: http://dx.doi.org/10.1016/j.apenergy.2011.04.059.

[35] H. Ren and W. Gao. Economic and environmental evaluation of micro CHP systems with different operating modes for residential buildings in japan. *Energy Build. 42(6),* pp. 853-861. 2010. . DOI: http://dx.doi.org/10.1016/j.enbuild.2009.12.007.

[36] L. Barelli, G. Bidini, F. Gallorini and A. Ottaviano. Dynamic analysis of PEMFC-based CHP systems for domestic application. *Appl. Energy 91(1),* pp. 13-28. 2012. . DOI: http://dx.doi.org/10.1016/j.apenergy.2011.09.008.

[37] A. A. Moghaddam, A. Seifi, T. Nikman, M.R.A. Pahlavani. Multi-objective operation management of a renewable MG (micro-grid) with back-up micro-turbine/fuel cell/battery hybrid power source. *Energy 36(11),* pp. 6490-6507. 2011. . DOI: http://dx.doi.org/10.1016/j.energy.2011.09.017.

[38] T. Hong, D. Kim, C. Koo and J. Kim. Framework for establishing the optimal implementation strategy of a fuel-cell-based combined heat and power system: Focused on multi-family housing complex. *Appl. Energy 127*pp. 11-24. 2014. . DOI: http://dx.doi.org/10.1016/j.apenergy.2014.04.018.

[39] S. Pellegrino, A. Lanzini and P. Leone. Techno-economic and policy requirements for the market-entry of the fuel cell micro-CHP system in the residential sector. *Appl. Energy 143*pp. 370-382. 2015. . DOI: http://dx.doi.org/10.1016/j.apenergy.2015.01.007.

[40] P. Jochem, M. Schönfelder and W. Fichtner. An efficient two-stage algorithm for decentralized scheduling of micro-CHP units. *Eur. J. Oper. Res. 245(3),* pp. 862-874. 2015. . DOI: http://dx.doi.org/10.1016/j.ejor.2015.04.016.

[41] M. Nazari-Heris, S. Abapour and B. Mohammadi-Ivatloo. Optimal economic dispatch of FC-CHP based heat and power micro-grids. *Appl. Therm. Eng. 114*pp. 756-769. 2017. . DOI: http://dx.doi.org/10.1016/j.applthermaleng.2016.12.016.

[42] M. Shahverdi and S. M. Moghaddas-Tafreshi. Operation optimization of fuel cell power plant with new method in thermal recovery using particle swarm algorithm. Presented at 2008 Third International Conference on Electric Utility Deregulation and Restructuring and Power Technologies. 2008, . DOI: 10.1109/DRPT.2008.4523839.

[43] A. D. Hawkes, D. J. L. Brett and N. P. Brandon. Fuel cell micro-CHP techno-economics: Part 1 – model concept and formulation. *Int J Hydrogen Energy 34(23),* pp. 9545-9557. 2009. . DOI: http://dx.doi.org/10.1016/j.ijhydene.2009.09.094.

[44] A. D. Hawkes, D. J. L. Brett and N. P. Brandon. Fuel cell micro-CHP techno-economics: Part 2 – model application to consider the economic and environmental impact of stack degradation. *Int J Hydrogen Energy 34(23),* pp. 9558-9569. 2009. . DOI: http://dx.doi.org/10.1016/j.ijhydene.2009.09.095.

[45] A. Arsalis, M. P. Nielsen and S. K. Kær. Modeling and optimization of a 1 kWe HT-PEMFC-based micro-CHP residential system. *Int J Hydrogen Energy 37(3),* pp. 2470-2481. 2012. . DOI: http://dx.doi.org/10.1016/j.ijhydene.2011.10.081.

[46] A. Adam, E. S. Fraga and D. J. L. Brett. Options for residential building services design using fuel cell based micro-CHP and the potential for heat integration. *Appl. Energy 138*pp. 685-694. 2015. . DOI: http://dx.doi.org/10.1016/j.apenergy.2014.11.005.

[47] F. Marechal, F. Palazzi, J. Godat and D. Favrat. Thermo-economic modelling and optimisation of fuel cell systems. *Fuel Cells 5(1),* pp. 5-24. 2005. . DOI: 10.1002/fuce.200400055.

[48] B. Najafi, A.H. Mamaghani, F. Rinaldi and A. Casalegno. Long-term performance analysis of an HT-PEM fuel cell based micro-CHP system: Operational strategies. *Appl. Energy 147*pp. 582-592. 2015. . DOI: http://dx.doi.org/10.1016/j.apenergy.2015.03.043.

[49] F. J. Asensio, J.I. San Martin, I. Zamora and J. García-Villalobos. Fuel cell-based CHP system modelling using artificial neural networks aimed at developing techno-economic efficiency maximization control systems. *Energy 123,* pp. 585-593. 2017. . DOI: http://dx.doi.org/10.1016/j.energy.2017.02.043.

[50] W. Huang, C. Yan, J. Wang and W. Wang. A time-delay neural network for solving time-dependent shortest path problem. Neural Networks 90, pp. 21-28. 2017.

[51] M. Mrugalski, M. Luzar, M. Pazera, M. Witczak and C. Aubrun. Neural network-based robust actuator fault diagnosis for a non-linear multi-tank system. ISA Trans. 61, pp. 318-328. 2016.

[52] R. Petrone, Z. Zheng, D. Hissel, M.C. Péra, C. Pianese, M. Sorrentino, M. Becherif and N. Yousfi-Steiner. A review on model-based diagnosis methodologies for PEMFCs. Int J Hydrogen Energy 38(17), pp. 7077-7091, 2013.

[53] Z. Zhong, X. Zhu and G. Cao. Modeling a PEMFC by a support vector machine. J. Power Sources 160(1), pp. 293-298, 2006.

[54] I. Han and C. Chung. Performance prediction and analysis of a PEM fuel cell operating on pure oxygen using data-driven models: A comparison of artificial neural network and support vector machine. Int J Hydrogen Energy 41(24), pp. 10202-10211. 2016.

[55] D.W. Manquardt, "An algorithm for least-squares estimation of nonlinear parameters, Journal of the Society for Industrial and Applied Mathematics", vol. 11 (2), pp. 431-441, 1963.

[56] C. Wang, S.S. Venkatesh, and J.S. Judd, "Optimal Stoping and Effective Machine Complexity Learning", Advances in Neural Information Processing Systems, Vol. 6, 303-310, 1994.

[57] G. K. Batchelor, *An Introduction to Fluid Dynamics.* Cambridge University Press, 2000.

[58] R. R. Panton, *Incompressible Flow.* Wiley & Sons, Inc., 2013.

[59] J. Spurk and N. Aksel, *Fluid Mechanics.* Springer, 2008.

[60] T. L. Bergman, A.S. Lavine, F.P. Incropera and D.P. Dewitt, *Fundamentals of Heat and Mass Transfer.* John Wiley & Sons Inc., 2011.

[61] A. Bejan, *Convection Heat Transfer.* John Wiley & Sons Inc., 2013.

[62] F. N. Fritsch and R. E. Carlson, "Monotone Piecewise Cubic Interpolation," *SIAM J. Numer. Anal.,* vol. 17, pp. 238-246, 1980.